JGR Solid Earth

RESEARCH ARTICLE
10.1029/2019JB017307

Constraints on Seismic Anisotropy in the Mantle Transition Zone From Long-Period SS Precursors

Quancheng Huang[1], Nicholas Schmerr[1], Lauren Waszek[2,3], and Caroline Beghein[4]

[1]Department of Geology, University of Maryland, College Park, MD, USA, [2]Research School of Earth Sciences, Australian National University, Acton, Australia, [3]Department of Physics, New Mexico State University, Las Cruces, NM, USA, [4]Department of Earth, Planetary, and Space Sciences, University of California, Los Angeles, CA, USA

Key Points:
- The MTZ anisotropy is investigated from the SS precursors at both regional and global scales
- We observe ~3% anisotropy in the MTZ beneath subduction zones but negligible MTZ anisotropy (<1%) at a global scale
- We propose a new MTZ topography model corrected for the upper mantle and MTZ anisotropy structures

Supporting Information:
- Supporting Information S1

Correspondence to:
Q. Huang,
qchuang@umd.edu

Citation:
Huang, Q., Schmerr, N., Waszek, L., & Beghein, C. (2019). Constraints on seismic anisotropy in the mantle transition zone from long-period SS precursors. *Journal of Geophysical Research: Solid Earth*, *124*, 6779–6800. https://doi.org/10.1029/2019JB017307

Received 6 JAN 2019
Accepted 9 JUN 2019
Accepted article online 24 JUN 2019
Published online 12 JUL 2019

Abstract The mantle transition zone (MTZ) of Earth is demarcated by solid-to-solid phase changes of the mineral olivine that produce seismic discontinuities at 410 and 660-km depths. Mineral physics experiments predict that wadsleyite can have strong single-crystal anisotropy at the pressure and temperature conditions of the MTZ. Thus, significant seismic anisotropy is possible in the upper MTZ where lattice-preferred orientation of wadsleyite is produced by mantle flow. Here, we use a body wave method, SS precursors, to study the topography change and seismic anisotropy near the MTZ discontinuities. We stack the data to explore the azimuthal dependence of travel-times and amplitudes of SS precursors and constrain the azimuthal anisotropy in the MTZ. Beneath the central Pacific, we find evidence for ~4% anisotropy with a SE fast direction in the upper mantle and no significant anisotropy in the MTZ. In subduction zones, we observe ~4% anisotropy with a trench-parallel fast direction in the upper mantle and ~3% anisotropy with a trench-perpendicular fast direction in the MTZ. The transition of fast directions indicates that the lattice-preferred orientation of wadsleyite induced by MTZ flow is organized separately from the flow in the upper mantle. Global azimuthal stacking reveals ~1% azimuthal anisotropy in the upper mantle but negligible anisotropy (<1%) in the MTZ. Finally, we correct for the upper mantle and MTZ anisotropy structures to obtain a new MTZ topography model. The anisotropy correction produces ±3 km difference and therefore has minor overall effects on global MTZ topography.

1. Introduction

The mantle transition zone (MTZ) is bounded by the 410 and 660-km discontinuities and plays an important role in mantle convection and global water circulation between upper and lower mantle (e.g., Bercovici & Karato, 2003). These major MTZ discontinuities are characterized by sharp seismic velocity and density jumps as a primary 1-D feature of the Earth (e.g., Dziewonski & Anderson, 1981). The boundaries are attributed to the pressure-induced phase changes of olivine with increasing pressure and temperature: olivine to wadsleyite at 410 km, wadsleyite to ringwoodite at 520 km, and ringwoodite to ferropericlase + bridgmanite at 660 km (Ita & Stixrude, 1992; Ringwood, 1975). The phase changes at 410 and 660 km have opposite Clapeyron slopes (Ito & Takahashi, 1989; Katsura & Ito, 1989); this results in a thinner MTZ in hot regions, and thicker MTZ in cold regions, assuming that pressure and temperature effects are dominant. The topography of MTZ discontinuities has previously been used successfully as a mantle thermometer to study thermal heterogeneities and map flow patterns (Bina & Helffrich, 1994; Gu et al., 1998; Helffrich, 2000; Stixrude, 1997).

Over the last two decades, the topography of MTZ discontinuities has been systematically mapped using various seismic methods, including SS and PP precursors (e.g., Flanagan & Shearer, 1998, 1999), ScS reverberations (e.g., Revenaugh & Jordan, 1991), and receiver functions (e.g., Lawrence & Shearer, 2006). SS precursors are the underside reflections of shear waves at the 410 and 660-km discontinuities (Figure 1). Measurements of SS precursors provided the first global-scale topography maps of the 410 and 660-km discontinuities (Chambers et al., 2005; Deuss & Woodhouse, 2002; Flanagan & Shearer, 1998; Gu & Dziewonski, 2002; Houser et al., 2008; Lawrence & Shearer, 2008; Shearer, 1991, 1993). Regional-scale SS precursor studies were performed for areas of high data density, including the Pacific Ocean (Cao et al., 2011; Schmerr et al., 2010; Schmerr & Garnero, 2006; Thomas & Billen, 2009; Yu et al., 2017), South America (Schmerr & Garnero, 2007), and central and eastern Asia (Heit et al., 2010; Lessing et al., 2014). Despite the discrepancies between topography models, deep 410-km and shallow 660-km discontinuities

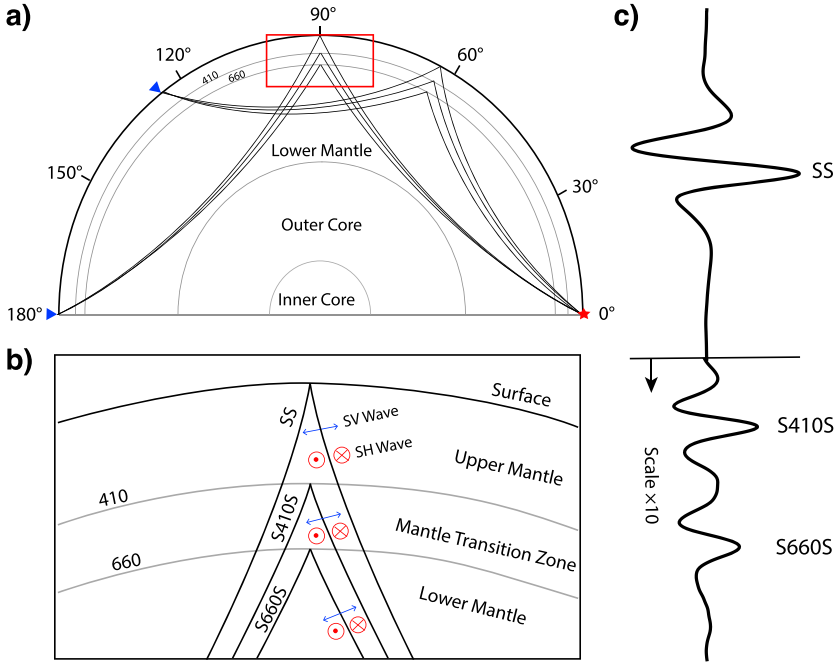

Figure 1. Example raypaths and seismograms of the SS precursors. (a) The raypaths of SS precursors at the epicentral distances of 125° and 180°. The red star represents the source, and blue triangles denote the stations. The reflections at the 410 and 660-km discontinuities are highlighted by the red box. (b) Expanded view of SS precursor raypaths beneath the bounce point region. The SS precursors reflected off 410 and 660-km discontinuities are named as S410S and S660S, respectively. The polarizations of SH and SV waves are plotted as red and blue arrows, respectively. This study focuses on using the SH waves to detect azimuthal anisotropy. (c) An example stacked seismogram of SS phase and the precursors.

(thin MTZ) are generally observed beneath hot mantle plume regions. Conversely, shallow 410-km and deep 660-km discontinuities (thick MTZ) are typically detected beneath cold subduction zones. This is consistent with the mineralogical properties of the phase changes. However, seismic anisotropy in the upper mantle and transition zone has not been previously taken into account when mapping the 410 and 660 depths, which may cause significant biases for MTZ topography measurements in a region with limited azimuthal coverage.

Seismic anisotropy describes the dependence of seismic velocity on the propagation or polarization directions of seismic waves. It is produced by two primary deformation mechanisms within the Earth: the lattice-preferred orientation (LPO) of anisotropic minerals or the shape-preferred orientations (SPO) of distinct isotropic materials. In the upper mantle, the LPO of olivine explains most observations of seismic anisotropy as olivine is the most volumetrically abundant mineral with ~18% of single-crystal shear wave anisotropy (Mainprice, 2007; Mainprice et al., 2005; Webb, 1989). In the transition zone, the orthorhombic wadsleyite has up to 14% single-crystal shear wave anisotropy (Sawamoto et al., 1984; Sinogeikin et al., 1998; Zha et al., 1997). Ringwoodite, present in the deeper MTZ, has a cubic structure and is nearly isotropic with only ~2% shear wave anisotropy (Kiefer et al., 1997; Li et al., 2006; Sinogeikin et al., 2003; Weidner et al., 1984). The abundant majorite garnet is also nearly isotropic in the transition zone (Bass & Kanzaki, 1990; Pamato et al., 2016). Clinopyroxene would not produce significant seismic anisotropy due to its low volume fraction in the MTZ (Sang & Bass, 2014). As a result, wadsleyite is the main candidate to generate seismic anisotropy in the upper part of the MTZ. Thus, we hypothesize that the LPO of wadsleyite caused by the deformation from mantle flow (e.g., upwelling plume or subducting slab) will produce seismic anisotropy in the MTZ. It should be noted that magnesite, with ~40% shear wave anisotropy, in the regionally carbonated mantle (e.g., subducted slabs) might be a candidate as well (Yang et al., 2014).

Seismic evidence of upper mantle anisotropy (<220 km) is widely reported in global tomography models (e.g., Beghein & Trampert, 2004; Chang et al., 2015; French & Romanowicz, 2014; Lekić & Romanowicz,

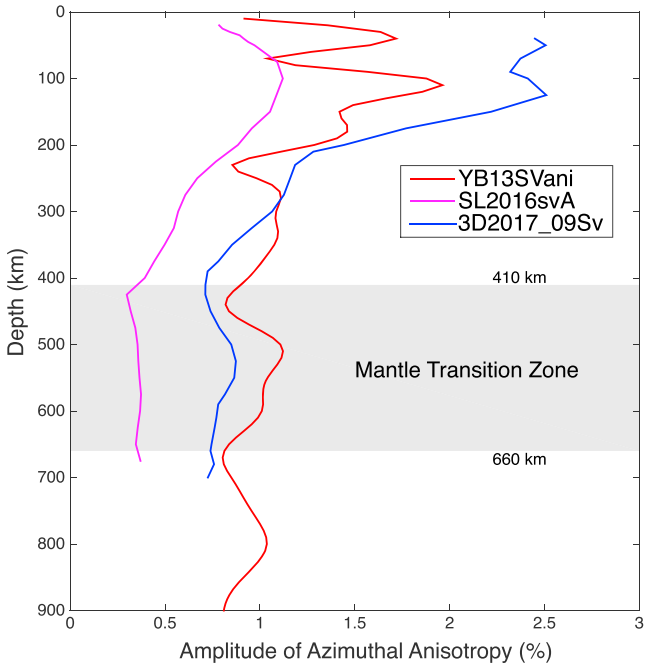

Figure 2. The root-mean-squares (RMS) of azimuthal anisotropy amplitudes from three surface wave anisotropy models: YB13SVani (Yuan & Beghein, 2013), SL2016svA (Schaeffer et al., 2016), and 3D2017_09Sv (Debayle et al., 2016) are plotted as a function of depth. The depth range of the MTZ (410–660 km) is highlighted in the gray box.

2011; Moulik & Ekström, 2014). However, observations of MTZ anisotropy are challenging due to the lower resolution and decrease in the strength of anisotropy at greater depths. Despite these difficulties, evidence for MTZ azimuthal anisotropy is provided by shear wave splitting measurements (Chen & Brudzinski, 2003; Foley & Long, 2011; Fouch & Fischer, 1996; Tong et al., 1994; Wookey et al., 2002), normal modes (Beghein et al., 2008), surface wave tomography (Debayle et al., 2016; Trampert & van Heijst, 2002; Yuan & Beghein, 2013, 2014, 2018), inversion of surface and *S* waveforms (Schaeffer et al., 2016), and the inversion of deep earthquake moment tensors (Li et al., 2018). For example, Trampert and van Heijst (2002) showed that Love wave overtones are compatible with the presence of azimuthal anisotropy in the MTZ. Wookey et al. (2002) found evidence for seismic anisotropy near the 660-km discontinuity beneath the Tonga-Kermadec subducting slabs using shear wave splitting, and this is interpreted as the mineral alignment by mid-mantle flow. Recently, Li et al. (2018) used the moment tensor of deep, non-double-couple earthquakes to invert for in situ seismic anisotropy assuming shear-dislocation faulting mechanism and found 25% anisotropy in the MTZ, which was explained with the presence of magnesite or carbonate melt.

In Figure 2, we compare the root-mean-squares (RMS) of azimuthal anisotropy amplitudes from three recent surface wave tomography models, which use higher modes of surface wave and thus are sensitive to the azimuthal anisotropy in the MTZ. In all three models, the strongest azimuthal anisotropy (~2%) exists in the upper mantle above 220 km. The YB13SVani (Yuan & Beghein, 2013) and 3D2017_09Sv (Debayle et al., 2016) models found ~1.0% and ~0.8% azimuthal anisotropy in the whole transition zone, respectively. However, the cross-model correlation of different surface wave tomography models in the MTZ is extremely low compared to their relatively good agreement in the upper mantle (Schaeffer et al., 2016). The coherence between surface wave tomography models and global SKS splitting measurements (Becker et al., 2012) is even lower in the MTZ. This implies that azimuthal anisotropy in the MTZ is not well constrained from either the surface wave or shear wave splitting methods.

In this study, we use a body wave method, SS precursors (SH wave), to constrain azimuthal anisotropy in the MTZ, via examining the azimuthal dependence of their travel-times and amplitudes. The SS precursor method has excellent data coverage in oceanic regions and a higher vertical resolution in the MTZ compared to shear wave splitting methods. This method has been previously applied to lithosphere-asthenosphere boundary (Rychert et al., 2012, 2014). Our study of MTZ anisotropy also provides corrections that contribute to a more precise MTZ topography model. These improved constraints on the MTZ anisotropy and topography structures illuminate the nature and style of mantle convection.

2. Methods

2.1. Data Set

Our study benefits from a global SS data set consisting of 45,624 seismograms (Waszek et al., 2018). The data set incorporates a global catalog of large earthquakes ($6 \leq M_w \leq 7$) from 1988 and 2016, to ensure significant SS signals above the background noise. The event depth criteria are shallower than 30 km to avoid interference with depth phases, with event-receiver epicentral distances between 100° and 180°. The data are filtered using a Butterworth band-pass filter between 15 and 50 s to remove seismic noise, and records with signal-to-noise ratio lower than 2.5 are discarded. Here, we use the transverse components (BHT) to study the SH waves for topography and azimuthal anisotropy in the MTZ. Predicted travel-times from the Preliminary Reference Earth Model (PREM) by Dziewonski and Anderson (1981) provide a time window to visually select the SS phase, which is handpicked. The polarities of SS phases are reversed to positive where necessary, and the seismograms are aligned to the peak maxima, then normalized.

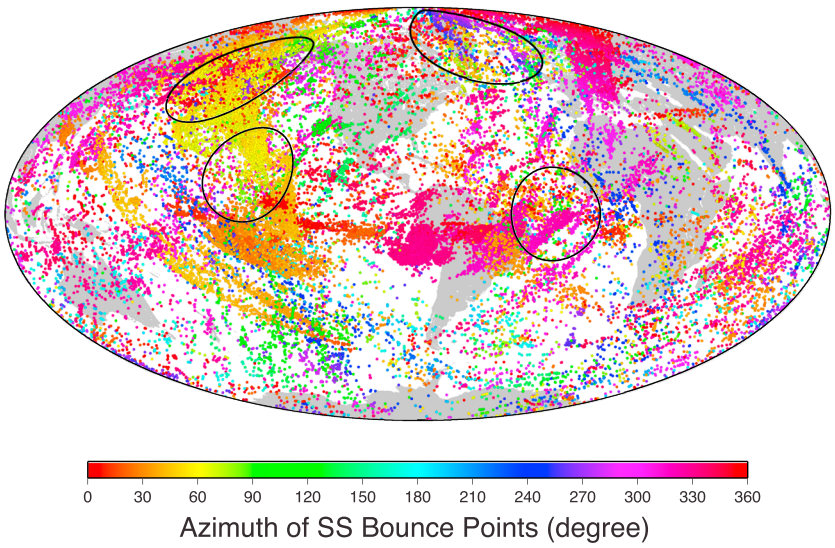

Figure 3. The map of SS bounce points in the SS data set. The colors represent the azimuths of SS bounce points, which point from the sources to receivers. The black circles highlight the four regions with ample bounce points and azimuthal coverage.

The SS precursors are sensitive to the structure beneath the bounce points (Figure 1) and provide dense sampling coverage in oceanic regions such as the northwestern and central Pacific (Figure 3). Our goal is to map the azimuthal variations of SS precursor travel-times and amplitudes as a function of bounce point azimuths. Thus, in addition to the number of records, we employ the azimuthal coverage criteria for selecting study regions to investigate azimuthal anisotropy in the MTZ. However, regions with high bounce point density tend to have uniform azimuthal distribution (e.g., South America and Indian Ocean) because most data are produced from similar event-receiver configurations. A global search for regions with both dense bounce points and sufficient azimuthal coverage identifies four suitable target locations to study azimuthal anisotropy: (1) the northwestern Pacific, (2) the central Pacific, (3) the central Atlantic, and (4) Greenland (Figure 3).

2.2. Stacking Methods

The amplitudes of SS precursors are only ~5% of SS phase, which require stacking to suppress noise and improve the signal-to-noise ratio. We follow the stacking method by Schmerr and Garnero (2006) to stack SS precursors along the predicted slowness curves, using 125° as the reference distance. We align the data to the predicted travel-times of SS precursors at the reference distance from PREM in order for coherent stacking. We use distance exclusion windows to avoid the interference of other seismic arrivals that have similar amplitudes with SS precursors and could contaminate our results. These phases with similar amplitudes include topside reflections (e.g., s660sS) and ScS reverberations (e.g., ScS660ScS). The exclusion windows for S410S are 0–100° and 135–145°; S660S windows are 0–115° and 165–180° (Schmerr & Garnero, 2006). The travel-times of SS precursors are then converted to depths using PREM. A bootstrap technique with 300 random resamples provides the 95% confidence level (2σ) of travel-times and amplitudes of the stacking results (e.g., Efron & Tibshirani, 1986).

We use different bin geometries to stack the data set: geographical bins and azimuthal bins. For the geographical bins, we place equally spaced 1,000-km radius bins that are overlapping every 500 km to map the topography of 410 and 660-km discontinuities. For the azimuthal stacks, we place 2,000-km radius geographical bins in the four target locations (Figure 3). We then further break down the records within the geographical bins to generate 30° azimuthal bins of the bounce point azimuths. The SS precursors traveling along one azimuth (e.g., α) are sensitive to the same velocity structure as those traveling in the opposite direction ($\alpha+\pi$). Consequently, we combine the two azimuthal bins with a π shift to improve the azimuthal sampling. This method provides regional estimates of MTZ anisotropy. A second technique for azimuthal stacking is used for data from subduction zones around the Pacific Ocean. Due to limited azimuthal

coverage in each subduction zone, we combine all the subduction zones into one data set and define a relative azimuth (Figure 7b). We then stack the subduction zone data according to the relative azimuths to explore MTZ anisotropy in the vicinity of subduction zones. Finally, we calculate the relative azimuths between bounce point azimuths and fast directions from global surface wave tomography models (e.g., Debayle et al., 2016; Schaeffer et al., 2016; Yuan & Beghein, 2013) for the entire data set. We stack the data into 15° bins of relative azimuths to study global azimuthal anisotropy patterns in the upper mantle and MTZ.

2.3. Crust and Tomography Corrections

The crustal thickness, surface topography, and upper mantle heterogeneities all affect the travel-times of SS and its precursors, biasing the measurements of MTZ topography and anisotropy. Thus, we apply pre-stacking crust and tomography corrections for each record, to remove the effects from isotropic crustal and upper mantle structures. For the crust, we use CRUST 2.0 model (Bassin et al., 2000) to calculate travel-time residuals beneath each bounce point with respect to PREM. Then, we use S40RTS tomography model (Ritsema et al., 2011) to correct for the lateral heterogeneities in the upper mantle. Using 1-D ray tracing, we compute the travel-time residuals for the SS phase and precursors (SdS) with respect to PREM. The SS-SdS differential travel-time residuals are used as the tomography corrections. The 1-D ray tracing approach does not account for the 3-D effects of raypaths such as the sensitivity kernels of SS phase and precursors. As a result, the ray-theoretical corrections potentially underestimate the effect of 3-D velocity structures, especially the small-scale structures, on the travel-times of SS phase and precursors (e.g., Bai et al., 2012; Koroni & Trampert, 2016; Zhao & Chevrot, 2003). This may cause as much as 5-km errors (<3 km in a well-sampled region) in the depths of MTZ discontinuities (Bai et al., 2012). A recent study by Koroni et al. (2017) suggests that a full waveform approach, including both the 3-D sensitivity kernels and boundary kernels, improves the accuracy of corrections for the mantle velocity structures and better constrains the MTZ topography. Here, we focus on the large-scale structures (>1,000 km) in the upper mantle and MTZ. Therefore, the ray-theoretical corrections can remove most of the large-scale heterogeneities and should be accurate enough for this study.

2.4. Inversion for Azimuthal Anisotropy

The azimuthal variations of SS precursor travel-times arise from the seismic anisotropy in the upper mantle and MTZ. Here, we build 1-D anisotropy models to quantify the strength and fast direction of azimuthal anisotropy from SS precursor travel-times. In a transversely isotropic medium with a horizontal symmetry axis, the velocity of vertically propagating SH wave is expressed as the following equations (Crampin, 1984; Montagner et al., 2000):

$$\rho V_{qSH}^2 = L - G_c \cos 2\psi - G_s \sin 2\psi \tag{1}$$

$$L = \rho V_{SV}^2 = \frac{1}{2}(C_{44} + C_{55}) \tag{2}$$

where V_{qSH} is the velocity of quasi-SH wave, ψ is the azimuth of wave propagation direction, L is a function of the isotropic SV wave velocity and can be expressed as elastic parameters C_{ij}, and $Gc = \frac{1}{2}(C_{55} - C_{44})$ and $Gs = C_{54}$ are the 2ψ azimuthal terms of L (Montagner & Nataf, 1986).

We use equations (1) and (2) to perform an inversion for Gc and Gs values from the observed SdS travel-times. To achieve this, we first build simple 1-D anisotropy models with constant Gc and Gs values in the upper mantle (80–220 km) and MTZ (410–660 km) to predict SdS travel-times. Then, we use a grid search method and chi-squared statistics to determine the best fitting model and quantify the 2σ uncertainties:

$$\chi^2 = \sum_{i=1}^{N} \frac{\left(t_i^{\text{obs}} - t_i^{\text{pre}}\right)^2}{\sigma_i^2} \tag{3}$$

where t_i^{obs} is the observed SdS travel-times, t_i^{pre} is the predicted SdS travel-times, σ_i is the standard deviations of observed travel-times, and N is the number of measurements. The fast direction (Θ) and strength of anisotropy (G) are calculated from the best fitting Gc and Gs values:

$$\Theta = \frac{1}{2}\arctan(G_s/G_c) \tag{4}$$

$$G = \sqrt{G_s^2 + G_c^2} \tag{5}$$

2.5. Amplitude Correction

The SS precursor amplitudes are sensitive to the impedance contrast at 410 and 660-km discontinuities and thus can be used to detect seismic anisotropy near the discontinuities. However, five different factors contribute to the amplitudes: (1) reflection coefficient at the discontinuity, (2) attenuation along the raypath, (3) geometrical spreading, (4) focusing and defocusing effects from stacking, and (5) radiation patterns from different focal mechanisms. Only the reflection coefficient is sensitive to seismic anisotropy near the MTZ discontinuities. Therefore, we apply a post-stacking amplitude correction based on synthetic data, to negate other influences. We generate a 1-D synthetic data set using GEMINI (Friederich & Dalkolmo, 1995) for ak135 model (Kennett et al., 1995). The synthetics are matched with corresponding data by depth and epicentral distance then processed and stacked following the same procedure as for the real data.

The radiation patterns for SS and SdS phases are similar and canceled out by taking the relative amplitude of SdS/SS. Subsequently, the stacked SdS/SS amplitudes can be expressed as a function of only four other factors:

$$A_{\text{data}}^{SdS/SS} = R_{SdS/SS}(\overline{\Delta})\cdot G\cdot Q\cdot F \tag{6}$$

where $R_{SdS/SS}$ is the true reflection coefficient at the discontinuity, $\overline{\Delta}$ is the average epicentral distance of the bin, G is geometrical spreading factor, Q is attenuation factor, and F is the focusing and defocusing factor from stacking. The SdS/SS amplitude in synthetic stacking result can be expressed as

$$A_{\text{syn}}^{SdS/SS} = R_{SdS/SS}^{\text{mod}}(\overline{\Delta})\cdot G\cdot Q\cdot \text{F} \tag{7}$$

where $R_{SdS/SS}^{\text{mod}}$ is the reflection coefficient in model ak135. We assume that the attenuation, geometrical spreading, and focusing and defocusing effects of data and synthetics are similar and thus can be removed. We also assume that the scaling factor of the reflection coefficient from the average epicentral distance ($\overline{\Delta}$) to the reference epicentral distance ($\Delta_{\text{ref}} = 125°$) is similar in data and synthetics. Based on equations (6) and (7), the true reflection coefficient at the discontinuity is then given as follows:

$$R_{SdS/SS}(\Delta_{\text{ref}}) = R_{SdS/SS}^{\text{mod}}(\Delta_{\text{ref}})\cdot\frac{A_{\text{data}}^{SdS/SS}}{A_{\text{syn}}^{SdS/SS}} \tag{8}$$

where Δ_{ref} is the reference epicentral distance 125°, $A_{\text{data}}^{SdS/SS}$ is the SdS/SS amplitude of data stacking result, and $A_{\text{syn}}^{SdS/SS}$ is the SdS/SS amplitude of synthetic stacking result. The reflection coefficient is recovered from the amplitude ratio of data over synthetic stacking results. After amplitude corrections, we use a similar method as the travel-time inversion to invert for the azimuthal anisotropy near the 410 and 660-km discontinuities.

Saki et al. (2018) investigated the feasibility of using the reflection coefficients of PP and SS precursors, particularly the polarity change of amplitudes, to detect seismic anisotropy and constrain the type of deformation mechanisms near the 410-km discontinuity. However, the polarity change of SS precursors only exists at short epicentral distance range (e.g., 30°–40°), which is not applicable for SS precursor stacks due to the triplications and extremely low amplitudes in the range. Here, we focus on the azimuthal dependence of SS precursor amplitudes, which are all above zero, rather than detecting the polarity reversals.

3. Results

3.1. MTZ Topography

After stacking the data in 1,000-km radius caps, we obtain global topography maps of 410 and 660 depths, and MTZ thickness (Figure 4), corrected for crustal and upper mantle velocity structures. The mean

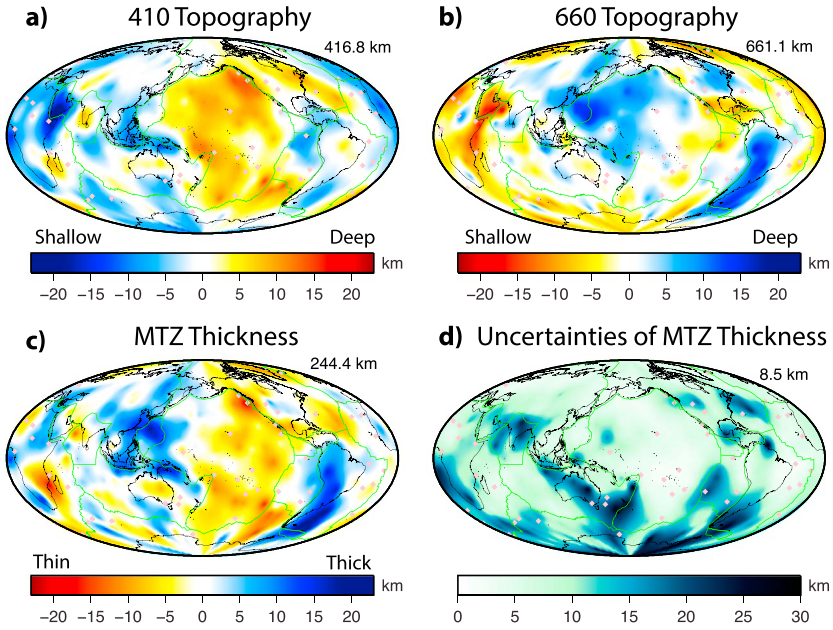

Figure 4. The MTZ topography model, which is corrected for crustal and upper mantle heterogeneities. The global map of (a) 410 topography, (b) 660 topography, (c) MTZ thickness, and (d) uncertainty of MTZ thickness. The average depths, thickness, and uncertainty are labeled on the top right corner of each panel. The pink dots denote the hot spots (Courtillot et al., 2003), and green lines are the plate boundaries (DeMets et al., 1990).

depths of 410 and 660-km discontinuities are 416.8 (±11.7) km and 661.1 (±11.9) km, respectively. The MTZ thickness is calculated as the difference between the 410 and 660 depths, with a mean value of 244.4 (±13.1) km. This value is independent from the upper mantle velocity structures and thus more robust than the individual 410 and 660 depths.

The 410 depth shows a strong depression beneath most of the Pacific Ocean (Figure 4a). This result is consistent with the presence of hotspots here, including Hawaii, Bowie, and Samoa, which can produce hot anomalies in the MTZ (e.g., Courtier et al., 2007). The 410 depth is slightly elevated beneath Sumatra and Philippine subduction zones, but no elevation is observed beneath Japan and South America subduction zones. A depression of the 660 depth is found beneath the subduction zones in the western Pacific (Japan, Izu-Bonin, Sumatra, and Tonga) and South America (Figure 4b). This corresponds well with cold anomalies introduced by the subducting slabs. The 660 depth is elevated beneath several hot spots such as Comoros, Iceland, and Bowie. Conversely, the 660 depths beneath Hawaii and southern Pacific hot spots are close to the global average.

Correspondingly, the MTZ thickness is characterized by thinning in the Pacific and thickening beneath the western Pacific and South America subduction zones (Figure 4c). A thinned MTZ is observed beneath most hot spots in Pacific (e.g., Hawaii, Bowie, Cobb, Samoa, and MacDonald), resulting mainly from the depressed 410-km discontinuity. In contrast, the thin MTZ beneath Iceland only arises from an elevation of the 660. The only thin MTZ region with both depressed 410 and elevated 660-km discontinuities is beneath the Comoros hot spot. A thickened MTZ beneath the western Pacific and South America subduction zones is primarily a consequence of the depression of 660-km discontinuity. The Sumatra subduction zone is the only thickened region to have both shallow 410-km and deep 660-km discontinuities. The MTZ thickness is generally thinned in the hot mantle plume regions and thickened in the cold slab regions. The general correlation of thick (thin) MTZ to cold (hot) regions indicates that mantle temperature plays a dominant role in MTZ topography.

The errors on MTZ thickness are closely related to the data coverage (Figure 4d). The uncertainties in the Southern Hemisphere are larger than the Northern Hemisphere due to inhomogeneous station density. Most of the oceanic regions (e.g., Pacific and Indian Oceans) and the Eurasia continent have ample data sampling (number of records, NR > 500) that yield an uncertainty less than 5 km. On the contrary, the

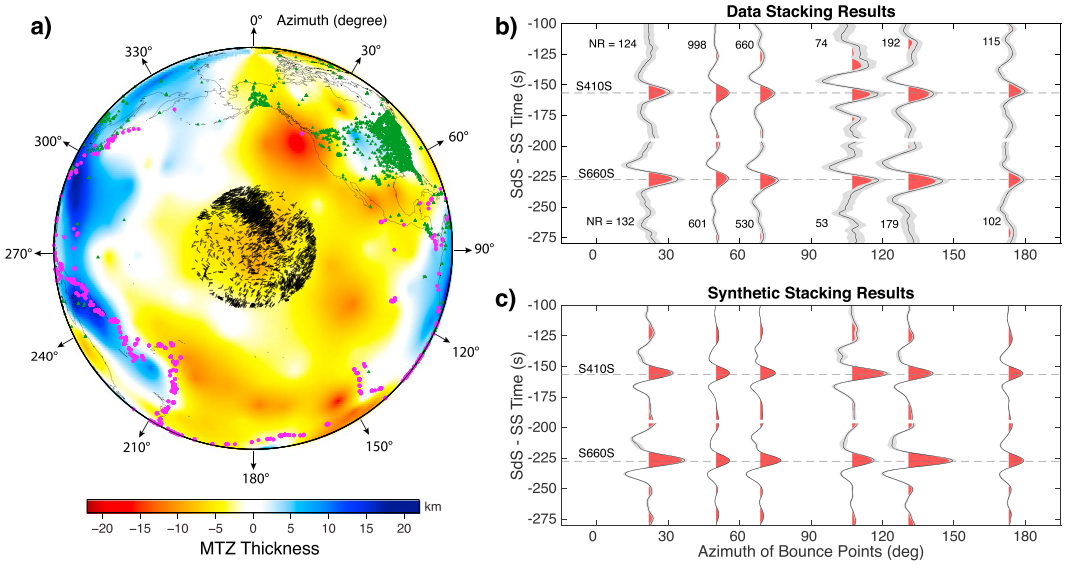

Figure 5. (a) The bounce point map of the central Pacific bin is superimposed on the map of MTZ thickness. The radius of the bin is 2,000 km. The black lines denote the bounce points and orientations of the SS raypaths. The pink circles and green triangles represent the earthquakes and stations, respectively. (b) The azimuthal stacking results of data in the central Pacific bin. The gray-shaded region is the 95% confidence levels of amplitudes estimated from bootstraps. The positive amplitudes are indicated in red. A gap is produced near −190 s because the S410S and S660S stacks are completed separately. The dash lines represent the average travel-times of S410S and S660S. The number of records (NR) of each stack are labeled beside the seismograms. (c) The azimuthal stacking results of corresponding synthetics.

data coverage in Australia, India, South Africa, and Argentina is poor (NR < 100) so the uncertainties are above 10 km.

The 10-km variation in topography is equivalent to ~3 s in travel-time variation. In order to constrain azimuthal anisotropy from SdS travel-times, we remove the effect of MTZ topography on the travel-times by applying a pre-stacking topography correction to the entire data set. From the topography calculated for 1,000-km radius bins, we compute the topography corrections from the difference between local 410, 660 depths and global mean values. We apply this correction prior to azimuthal stacking, ensuring that the azimuthal variations of SdS travel-times are independent from MTZ topography.

3.2. Regional Azimuthal Stacking

3.2.1. Central Pacific

The central Pacific bin is located near Hawaii, and the radius is 2,000 km (Figure 5a). Here, global stacks reveal that the MTZ thickness is thinned by ~10 km beneath Hawaii. The azimuths of bounce points are dominated by those oriented toward the USArray (30°–60°), but the southeast direction (90°–120°) is not well covered by the data. The data are stacked into 30° azimuthal bins (Figure 5b). The travel-time variations of S410S and S660S have less than 1-s deviation from the mean values. The amplitude variations are highly correlated with the 1-D synthetics (Figure 5c), indicating that most anomalies arise from attenuation and geometrical spreading, rather than azimuthal anisotropy at the discontinuities, and thus are removed by the amplitude corrections.

Considering the travel-times and amplitudes of SS precursors as a function of bounce point azimuths (Figure 6), we find that the S410S travel-time is sensitive to the upper mantle structure (0–410 km) and S660S travel-time is sensitive to both the upper mantle and transition zone structure (0–660 km). The upper mantle anisotropy is mapped onto both SS precursors due to the SS reference phase. However, the differential S410S-S660S travel-time is only affected by the transition zone structure (410–660 km), making it an independent indicator for MTZ anisotropy.

We build 1-D anisotropy models in both the upper mantle (80–220 km) and MTZ (410–660 km) to invert for the strength of anisotropy (dlnG = G/L) and fast direction (Θ) (Figure 6). The upper mantle model is applied to S410S and S660S travel-times and the MTZ model to the S410S-S660S travel-time and amplitude inversions. The best fitting model of S410S time is dlnG = 4.0 ± 3.2% and Θ = 95° ± 21° (Figure 6a). We find

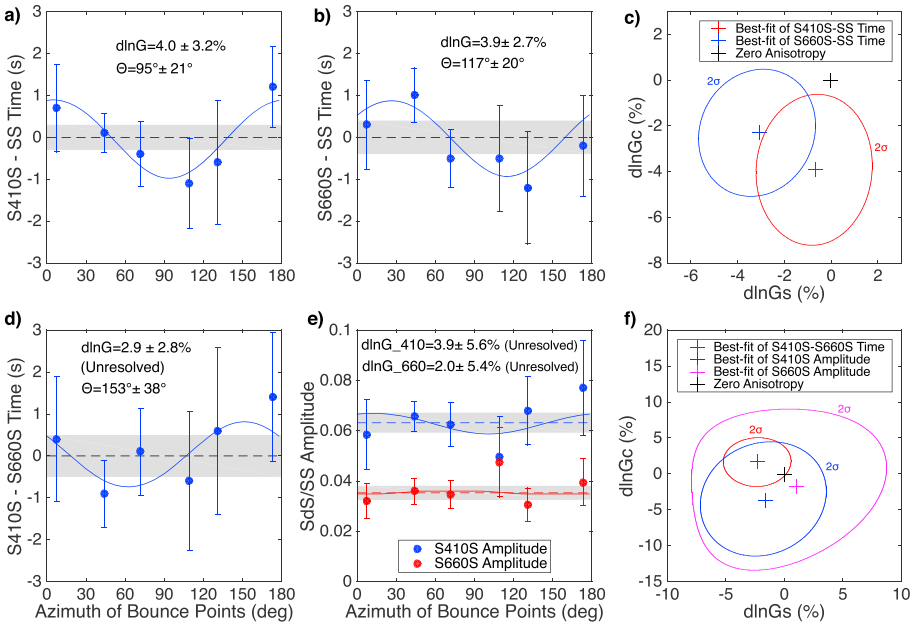

Figure 6. The measurements of relative travel-times and amplitudes of SS precursors in the central Pacific bin are plotted as a function of bounce point azimuths. (a) The S410S-SS travel-time residuals. The dash line is average travel-time measured from the stacking of all data in the central Pacific bin, and the gray-shaded box denotes the uncertainty. The blue curve is the best fitting model inverted from the 1-D anisotropy model. The dlnG and Θ values represent the strength of anisotropy and fast direction of the best fitting model, respectively. (b) The S660S-SS travel-time residuals. (c) The 2σ error ellipses of the best fitting models of S410S and S660S times estimated from the chi-squared statistics. The black cross denotes the zero anisotropy point. (d) The S410S-S660S travel-time residuals. (e) The S410S/SS (blue) and S660S/SS (red) amplitudes. (f) The 2σ error ellipses of the best fitting models of S410S-S660S time, S410S amplitude, and S660S amplitude.

that the fast direction is oriented southeast; this result is consistent with surface wave anisotropy models at 150-km depth (e.g., dlnG = 3.1%, Θ = 102° in Yuan & Beghein, 2013) and APM models (e.g., Θ = 155° in Becker et al., 2015) in the central Pacific region. The best fitting model for S660S time is dlnG = 3.9 ± 2.7% and Θ = 117° ± 20° (Figure 6b). The strength of anisotropy is consistent with the S410S inversion, but the fast direction is more southeasterly due to the bias from the MTZ structure. The 2σ error ellipses of S410S and S660S times do not include the zero anisotropy point (Figure 6c); this means that the strength of anisotropy in the upper mantle is significantly above zero.

Our inversion result of S410S-S660S time beneath the central Pacific bin is dlnG = 2.9 ± 2.8% and Θ = 153° ± 38° (Figure 6d). This indicates ~3% anisotropy existing in the MTZ here, and the fast direction is again oriented southeast. However, this value is not significantly above zero (Figure 6f) indicating that the MTZ anisotropy is not well resolved, in agreement with the uncertainty estimates of Yuan and Beghein (2018). Future work with additional data and less noisy stacks can help reduce the uncertainties of travel-time measurements and perhaps resolve the structure. The inversion results of S410S and S660S amplitudes are also not significantly above zero, and the 2σ errors are quite large compared to the S410S-S660S time (Figures 6e and 6f). We also examine the stacking results in the northwestern Pacific, Greenland, and central Atlantic but do not find significant signals for MTZ anisotropy (Figures S1–S3 in the supporting information).

3.2.2. Subduction Zones

Subducting slabs can introduce strong mantle flow into the MTZ and cause azimuthal anisotropy (e.g., Billen, 2008). Unfortunately, the SS data set does not have sufficient azimuthal coverage in any individual subduction zone to perform single-region studies. Thus, to explore the presence of azimuthal anisotropy near slabs, we select six subduction zones around the Pacific Ocean using the SLAB 1.0 model (Hayes et al., 2012): (1) Kamchatka/Japan/Izu-Bonin, (2) Aleutian, (3) Cascadia, (4) South America, (5) Kermadec-Tonga, and (6) Sumatra (Figure 7). We select the SS bounce points that are located beneath the slab contours defined by SLAB 1.0 model. Then, we define a new coordinate system using the trench-perpendicular and parallel directions to combine the six subduction zones into one data set (Figure 7b).

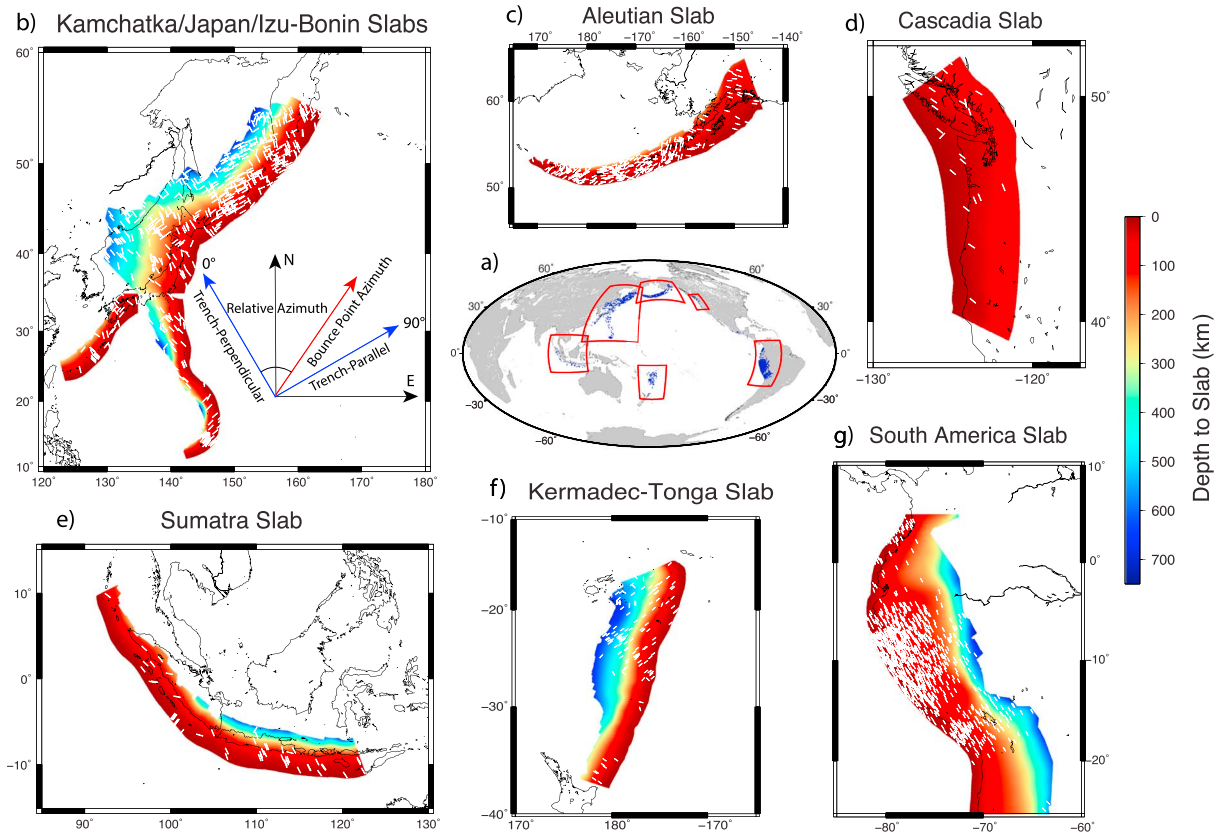

Figure 7. SS precursor azimuthal sampling in subduction zones. The geometries of slabs are from SLAB 1.0 model (Hayes et al., 2012). (a) The global map of bounce points in subduction zones. The blue points denote the bounce points, and the red boxes highlight the locations of six subduction zones. The six subduction zones are (b) Kamachatka/Japan/Izu-Bonin slabs and the illustration of the trench-perpendicular/parallel coordinate system; (c) Aleutian slab; (d) Cascadia slab; (e) Sumatra slab; (f) Kermadec-Tonga slab; (g) South America slab. The color bar shows the depth to slab, and the white vectors denote the azimuths of the bounce points.

We then calculate the relative azimuths between bounce point azimuths and trench perpendicular directions. We stack the whole subduction zone data set by relative azimuths into 30° bins. The stacking results are plotted as a function of relative azimuths (Figure 8); the 0° and 180° represent the trench-perpendicular direction, and the 90° represents the trench parallel direction.

The S410S travel-time (Figure 8a) has stronger variations than the S660S travel-time (Figure 8b). We use the 1-D anisotropy model (80–220 km) to invert for the upper mantle anisotropy, finding a best fitting model of S410S time as dlnG = 4.3 ± 2.4% and Θ = 100° ± 17°. This suggests that ~4% azimuthal anisotropy exists in the upper mantle beneath subduction zones with a nearly trench-parallel fast direction. The dlnG value inverted from S410S time is significantly above zero, while the one from S660S time is not significant (Figure 8c), which indicates that strong perturbations are caused by the MTZ structures beneath subduction zones.

The best fitting model of S410S-S660S time is dlnG = 2.7 ± 2.5% and Θ = 168° ± 33° (Figure 8d). It suggests that ~3% anisotropy exists in MTZ beneath subduction zones with a nearly trench-perpendicular fast direction. The strength of anisotropy is slightly weaker than the upper mantle, in agreement with the weaker elastic anisotropy of wadsleyite and ringwoodite compared to olivine. The fast direction transitions from trench parallel in the upper mantle into trench perpendicular in the MTZ, indicating that there could be a change of mantle flow direction with depth. The S410S and S660S amplitudes showed strong variations with relative azimuths, but they exhibited a higher correlation than other stacks ($r^2 = 0.67$). This may result from uncorrected 3-D attenuation structures in the upper mantle, which map SS amplitude variations onto S410S and S660S amplitudes. Thus, we further correct the correlated components between S410S and S660S amplitudes. After correction, neither of S410S and S660S shows significant variations with relative azimuths,

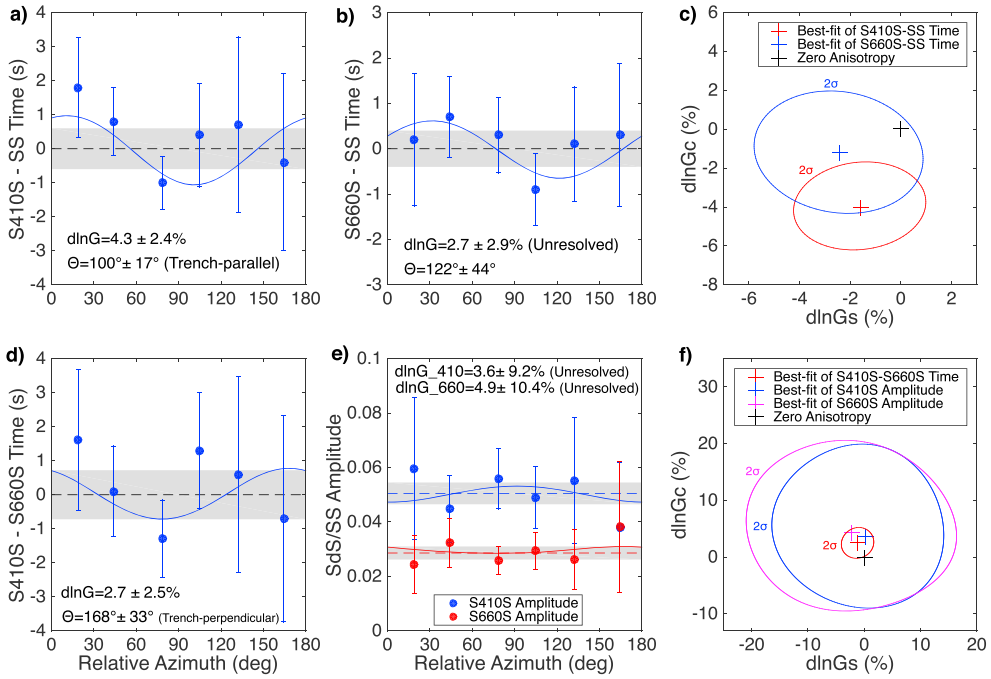

Figure 8. The azimuthal stacking results of subduction zones. (a) S410S travel-time residuals; (b) S660S travel-time residuals; (c) The 2σ error ellipses of the best fitting models of S410S and S660S times; (d) S410S-S660S travel-time residuals; (e) S410S and S660S amplitudes; (f) The 2σ error ellipses of the best fitting models of S410S-S660S time, S410S amplitude, and S660S amplitude. The legends are the same as Figure 6. The 0° and 180° represent the trench-perpendicular direction, and the 90° represents trench-parallel direction.

which indicates that no strong anisotropy exists near MTZ discontinuities (Figure 8e). The dlnG value inverted from S410S-S660S time is slightly above zero, while the amplitudes are not significant and have large uncertainties (Figure 8f).

3.3. Global Azimuthal Stacking

The regional azimuthal stacks are limited to locations with sufficient azimuthal coverage. Here, we also interrogate the upper mantle and MTZ anisotropy at a global scale. In surface wave anisotropy models, the fast directions change as a function of depth at any given location. We therefore compute an average anisotropy model across a certain range of depths (e.g., 410–660 km) for the global azimuthal stacking. We follow the methods of Montagner et al. (2000) to compute the synthetic shear wave splitting models from surface wave models:

$$\delta t = \sqrt{\left(\int_{h_1}^{h_2} \frac{G_c(z)}{V_s(z)L(z)}dz\right)^2 + \left(\int_{h_1}^{h_2} \frac{G_s(z)}{V_s(z)L(z)}dz\right)^2} \tag{9}$$

$$\phi = \frac{1}{2}\arctan\left(\frac{\int_{h_1}^{h_2} \frac{G_s(z)}{V_s(z)L(z)}dz}{\int_{h_1}^{h_2} \frac{G_c(z)}{V_s(z)L(z)}dz}\right) \tag{10}$$

where δt is the shear wave splitting time, ϕ is the fast direction, z is the depth, h_1 and h_2 are the lower and upper bounds of the depth range, and V_s is the shear wave velocity. We select two depth ranges to calculate the synthetic shear wave splitting models: (1) 80–220 km (upper mantle) and (2) 410–660 km (MTZ). We use the fast directions of the synthetic shear wave splitting model as an average model in these two depth ranges. The relative azimuths between the bounce point azimuths and averaged fast directions for the global azimuthal stacking allow us to examine the evidence of azimuthal anisotropy in the upper mantle and MTZ at a global scale.

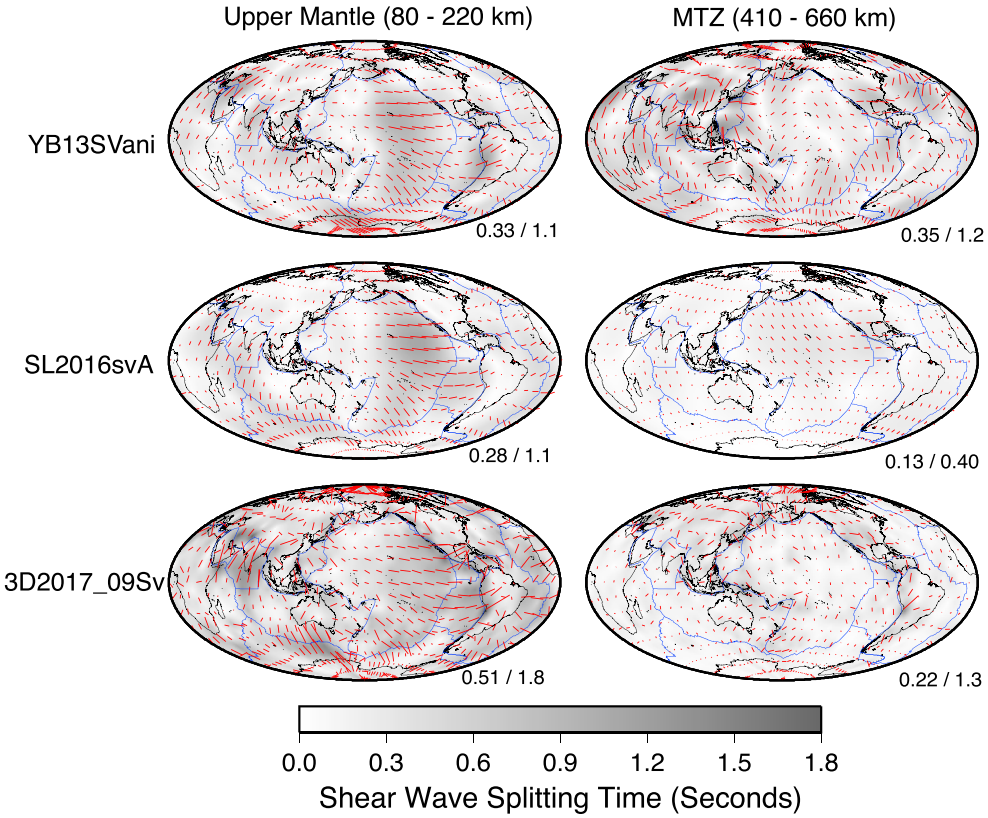

Figure 9. The depth-averaged shear wave splitting models computed from the surface wave anisotropy models: YB13SVani (Yuan & Beghein, 2013), SL2016svA (Schaeffer et al., 2016), and 3D2017_09Sv (Debayle et al., 2016). The first and second columns represent the models for the upper mantle (80–220 km) and MTZ (410–660 km), respectively. The red vectors denote the fast directions of azimuthal anisotropy, and the length is scaled with the strength of anisotropy. The numbers on the bottom right of each panel denote the mean/maximum shear wave splitting time. The fast directions of shear wave splitting models are used for global azimuthal stacking. The blue lines are the plate boundaries (DeMets et al., 1990).

The synthetic shear wave splitting models are computed from three surface wave anisotropy models using equations (9) and (10) (Figure 9). In the upper mantle, the fast directions are generally consistent in three models although 3D2017_09Sv model shows stronger anisotropy. In the MTZ, YB13SVani is the only model with relatively strong anisotropy compared to the upper mantle structure. Moreover, the fast directions from the three models are inconsistent, implying that the MTZ anisotropy is not well resolved from surface waves. We compute the relative azimuths of SS bounce points from the fast directions, in a similar way to the subduction zone data subsets. Benefitting from sufficient azimuthal coverage, we stack the global data set into 15° bins according to relative azimuth.

3.3.1. Upper Mantle

Upper mantle anisotropy affects the travel-times of SS phase, which are mapped onto the S410S and S660S travel-times. If the fast directions from the surface wave models are consistent with the Earth's anisotropy structures, we expect to observe a fast direction from SS precursors to be close to 0° or 180°. We inverted the observed travel-times and amplitudes for the fast direction (Θ) and strength of anisotropy (dlnG) in the upper mantle assuming a 1-D anisotropy model like we did in regional studies (Figure 10).

The S410S times show a clear 2ψ azimuthal variation, and the fast directions are close to 0° or 180° (Figures 10a–10c). This supports the concept that the fast directions in the upper mantle are well constrained from three surface wave models. The strengths of upper mantle anisotropy inverted from YB13SVani, SL2016svA, and 3D2017_09Sv models are dlnG = 0.95 ± 0.55%, dlnG = 0.91 ± 0.68%, and dlnG = 1.3 ± 0.3%, respectively. The dlnG values from three models are all significantly above zero (Figure 10g), suggesting that ~1% azimuthal anisotropy exists between 80 and 220 km in the upper mantle. This is weaker than

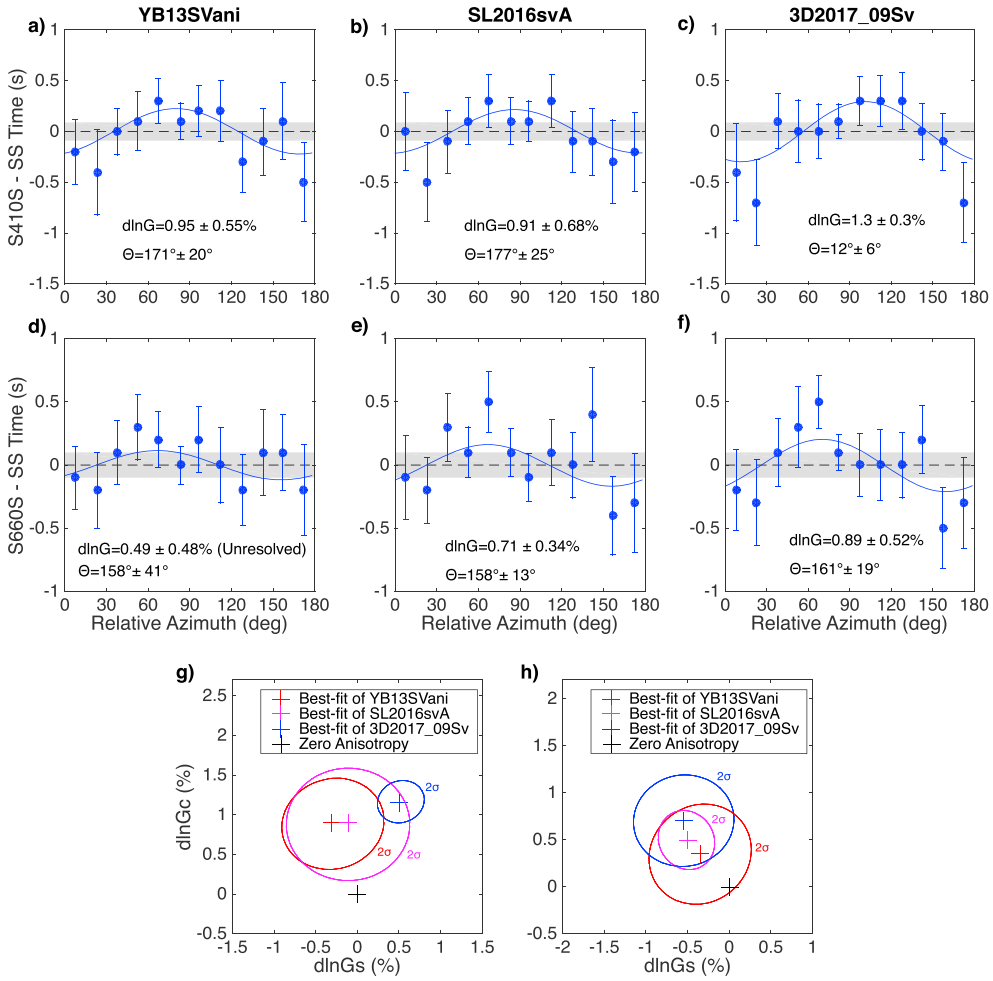

Figure 10. The global azimuthal stacking results for the upper mantle anisotropy. (a–c) The S410S travel-time residuals plotted as a function of relative azimuths, which are computed from the fast directions of three surface wave models. (d–f) The S660S travel-time residuals plotted as a function of relative azimuths. The legends are the same as Figure 6. The strength of anisotropy (dlnG) and fast direction (Θ) of the best fitting model is labeled in each panel. The 2σ error ellipses of the best fitting models of (g) S410S times and (h) S660S times.

the RMS amplitudes of azimuthal anisotropy in YB13SVani and 3D2017_09Sv model but stronger than SL2016svA model (Figure 2).

The S660S times produce more outliers than S410S times; these outliers are excluded from the inversions because they may be contaminated by MTZ structures (Figures 10d–10f). The best fitting S660S fast directions are close to 160° in all three surface wave models, which is ~20° from the predicted 180° fast direction. The dlnG values for YB13SVani, SL2016svA, and 3D2017_09Sv models are dlnG = 0.49 ± 0.48%, dlnG = 0.71 ± 0.34%, and dlnG = 0.89 ± 0.52% respectively. The dlnG value from YB13SVani is not significantly above zero, but the other two models are both significant (Figure 10h). The S660S times also support that ~1% azimuthal anisotropy exists in the upper mantle although the Θ and dlnG values may be inaccurate due to the contamination of uncorrected MTZ heterogeneities.

In summary, the upper mantle anisotropy is resolvable from S410S and S660S times for global azimuthal stacking. We find that the average strength of anisotropy is ~1% in the upper mantle (80–220 km), which is weaker than the estimates from surface waves. However, the strength of anisotropy is dependent on the thickness of the upper mantle model used for inversion, and the body wave method is intrinsically different from surface waves. To the first order, the upper mantle anisotropy from SS precursors is consistent with the surface wave models. However, our result suggests that the S410S and S660S travel-times can be biased by

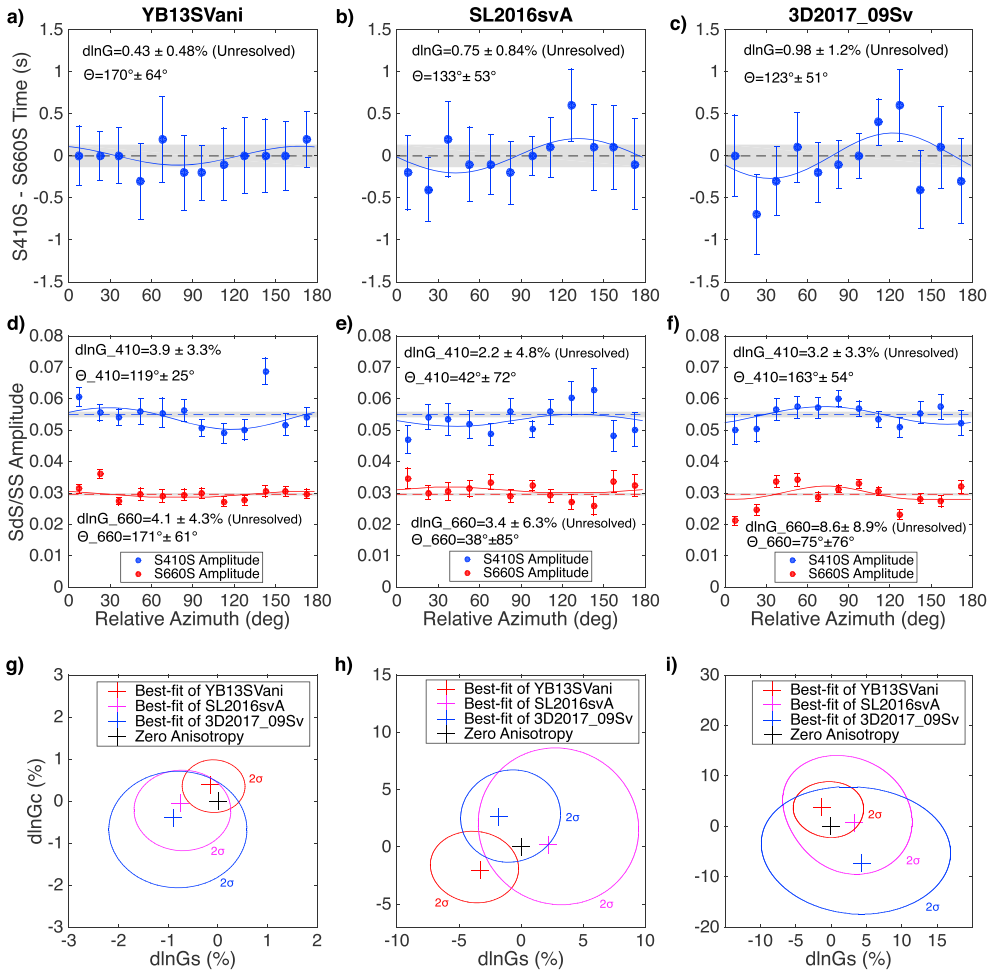

Figure 11. The global azimuthal stacking results for the MTZ anisotropy. (a–c) The S410S-S660S travel-time residuals plotted as a function of relative azimuths. (d–f) The S410S/SS (blue) and S660S/SS amplitudes (red) plotted as a function of relative azimuths. The 2σ error ellipses of the best fitting models of (g) S410S-S660S time, (h) S410S amplitude and (i) S660S amplitude in the MTZ. The legends are the same as Figure 6.

~0.5 s from upper mantle anisotropy, motivating an anisotropy correction to obtain more accurate 410 and 660 depths.

3.3.2. Mantle Transition Zone

We continue our experiments using global anisotropy models to stack for the structures in the MTZ. The S410S-S660S times and S410S, S660S amplitudes are the measurements sensitive to MTZ anisotropy. Considering these parameters as a function of relative azimuths (Figure 11), we find that the S410S-S660S times have weaker variations (Figures 11a–11c) than the upper mantle stacks. The dlnG values for YB13SVani, SL2016svA, and 3D2017_09Sv models are dlnG = 0.43 ± 0.48%, dlnG = 0.75 ± 0.84%, and dlnG = 0.98 ± 1.2%, respectively. None of the three models shows significant anisotropy signals above zero (Figures 11a–11c and 11g), which can be attributed to the poorly constrained anisotropy in the surface wave models. Alternatively, extremely weak anisotropy in the MTZ caused by the weak single-crystal anisotropy of wadsleyite and ringwoodite can explain this as well.

Figures 11d–11f reveal that the S410S and S660S amplitudes are close to the mean values and do not show a clear 2ψ variation after the amplitude corrections, except several outliers that are excluded from the inversions. The S410S and S660S amplitudes are correlated with each other in the SL2016svA model ($r^2 = 0.65$) indicating that the variations could result from the SS amplitude changes. We correct for the correlated component between S410S and S660S amplitudes. Only the dlnG value of S410S amplitude from YB13SVani model, dlnG = 3.9 ±3.3%, is significantly above zero (Figure 11d). However, the fast direction,

$\Theta = 119° \pm 25°$, is nearly perpendicular to the predicted 180° fast direction, which suggests that this signal is not well constrained. None of the other dlnG values is significantly above zero from the three surface wave models (Figures 11h and 11i). This result indicates that no strong anisotropy exists at 410 and 660-km discontinuities at the global scale.

Overall, we find that the MTZ anisotropy inverted from the global stacking approach is relatively weak; if it exists, it is less than 1%. It is difficult to quantify a small amount of anisotropy from S410S to S660S travel-times alone. Furthermore, the S410S and S660S amplitudes cannot resolve the anisotropy near 410 and 660-km discontinuities at the global scale, suggesting that signals are isolated to regional structures.

4. Discussion

4.1. Weak MTZ Anisotropy

In the global azimuthal stacking, we find evidence for ~1% azimuthal anisotropy in the upper mantle (80–220 km). We stack the global data set using the patterns of surface wave anisotropy at the depth range of crust (0–40 km) and deep upper mantle (220–410 km) but do not find a coherent anisotropy signal from the stacks. This indicates that the anisotropy arises from the shallow upper mantle (80–220 km). The LPO of olivine induced by the shear deformations is the most likely contribution to ~1% anisotropy in the asthenosphere (e.g., Karato et al., 2008). We divide the global data set into oceanic and continental sub-data sets to study the heterogeneities of anisotropy structures beneath oceans and continents in the asthenosphere. Our observations reveal that oceanic regions are consistent with the global average of ~1% anisotropy (Figure S4). However, the continental regions do not display a significant signal of anisotropy in the asthenosphere (Figure S5). Consequently, the global average is likely dominated by oceanic regions. We also test the SL2016svAr model by Schaeffer et al. (2016), which has smaller-scale variations and larger amplitudes, and we find similar results compared to the SL2016svA model.

We find that azimuthal anisotropy in the MTZ is weaker than 1% at the global scale. It is still uncertain that the non-detection of global MTZ anisotropy arises from using unconstrained surface wave anisotropy models as a reference or simply by weak anisotropy in the MTZ. The global azimuthal stacking is dependent on the fast directions of surface wave models; hence, the anisotropy signal is canceled if the fast directions are not accurate. On the other hand, the extremely weak anisotropy in the MTZ could be responsible for the non-detection. From a mineral physics perspective, it is debated that the LPO of wadsleyite is strong enough to produce detectable seismic anisotropy, even if it has relatively strong single-crystal anisotropy (~14%). For example, the mineral physics modeling predicts that a polycrystal of pyrolitic composition (60% wadsleyite, 40% garnet) under the shear strain of mantle flow can produce ~1% seismic anisotropy in the MTZ (Kawazoe et al., 2013; Tommasi et al., 2004). However, a recent mineral physics study by Zhang et al. (2018) suggests that 1% or more anisotropy in the MTZ cannot be explained by the LPO of wadsleyite as a primary source. They propose other mechanisms such as metastable olivine or SPO to explain observations of more than 1% anisotropy in the MTZ. Moreover, the mineral recrystallization of olivine at 410-km during the phase change to wadsleyite would also cause the loss of seismic anisotropy in the MTZ (Karato, 1988). Our observations with SS precursors are consistent with Zhang et al. (2018), which do not support more than 1% azimuthal anisotropy in the MTZ. This result contrasts with observations from surface waves that found that more than 1% azimuthal anisotropy could exist in the MTZ (e.g., Yuan & Beghein, 2013). However, given that uncertainties in global surface wave tomography can be quite large (Yuan & Beghein, 2018), and intrinsic discrepancies between body waves and surface waves, it would be difficult to compare them directly.

4.2. Mantle Flow in the MTZ

The MTZ anisotropy is weak at a global scale but could be regionally enhanced near strong mantle flow such as hot spots or subduction zones. In regional stacks of the central Pacific, we find evidence for ~4% azimuthal anisotropy in the upper mantle but no significant anisotropy in the MTZ. Surface wave studies reported upper mantle anisotropy in the central Pacific region (e.g., Ekström & Dziewonski, 1998; Montagner, 2002; Nishimura & Forsyth, 1989), including the three surface wave anisotropy models used in this study. Our observation of upper mantle anisotropy is consistent with the LPO fabrics of olivine induced by the horizontal mantle flow beneath Hawaii. However, the mantle plume mainly produces vertical flow in the MTZ, which cannot result in strong azimuthal anisotropy of SH wave (e.g., Tommasi et al., 2004). Thus, we would not expect a strong azimuthal anisotropy signature in the MTZ beneath plume regions.

Subducting slabs can introduce horizontal flow into the MTZ and may be a source of stronger azimuthal anisotropy. Beneath the subduction zones in this study, we find evidence for ~4% anisotropy in the upper mantle with a trench-parallel fast direction and ~3% anisotropy in the MTZ with a trench-perpendicular fast direction. The trench-parallel fast direction in the upper mantle is consistent with the observations by shear wave splitting measurements; for example, Long and Silver (2008, 2009) found that trench migration induced dominantly trench-parallel flow and anisotropic directions in the subslab mantle. However, other studies show that the fast directions in the mantle wedge are complicated in some areas, with a transition from trench-parallel in the fore-arc to trench-perpendicular in the back-arc (Long & Wirth, 2013). This may be caused by a combination of trench-perpendicular corner flow and B-type olivine or serpentinite minerals in the mantle wedge. However, the trench-parallel fast direction observed by our study of SS precursors is an average summation of the mantle wedge and subslab mantle structure and may not be sensitive to a smaller-scale transition of fast direction in the mantle wedge. Our result indicates that trench-parallel mantle flow is dominant in the upper mantle at the vicinity of subducting slabs.

A complication in interpreting our observations is that stacking produces an average result combining six subducting slabs with various velocity anomalies, thickness, dipping angles, and convergence directions at the trench. The stacking of data across multiple subduction zones would average out any local anisotropic structures that may dominate in a particular slab configuration. For example, the slabs with shallower dipping angles may cause stronger horizontal flow in the MTZ or have larger effects of SPO and thus contribute more to our anisotropy measurements over more vertically oriented slabs. Furthermore, the plate motion convergence directions are not always trench perpendicular (e.g., Becker et al., 2015), which increases the uncertainties of measured fast directions and strength of anisotropy. Since we focus on the coherent mantle flow pattern across different subduction zones, these incoherent structures would cancel out or contribute to the uncertainties in the stacks.

Despite these uncertainties, it is intriguing to find that the fast direction transitions from trench parallel in the upper mantle into trench perpendicular in the MTZ. Very few shear wave splitting studies have found evidence for the MTZ anisotropy (e.g., Chen & Brudzinski, 2003; Fouch & Fischer, 1996; Wookey et al., 2002), although one study detected a trench-parallel fast direction beneath the Tonga slab (Foley & Long, 2011). The surface wave models reveal a complicated pattern for the MTZ anisotropy beneath subduction zones. For example, the YB13SVani model (Yuan & Beghein, 2013) reports a trench-perpendicular fast axis beneath the Japan and Aleutian slabs but a trench-parallel fast axis beneath the South America slab (Figure 9). We note, however, that the lateral resolution of such models is lower than that necessary to resolve a subducting slab. Our results suggest that the trench-perpendicular mantle flow becomes dominant in the MTZ beneath subduction zones. As subducting slabs descend into the mid-mantle, they can either penetrate through the MTZ or stagnate at the bottom of the MTZ (e.g., Fukao et al., 2001). The trench-perpendicular fast axis better agrees with the mantle flow field caused by stagnant slabs in the MTZ (e.g., Billen, 2010); thus, our signals may be dominated by stagnant slabs (e.g., Japan). However, because of uncertainties on the effect of pressure, water, or recrystallization across the MTZ boundaries on seismic anisotropy, we cannot rule out that mantle flow direction remains constant with depth and that we are seeing the signature of these other factors on the anisotropy (Yuan & Beghein, 2013). Additionally, other mechanisms such as the SPO produced within slabs and different slip systems of wadsleyite (e.g., Kawazoe et al., 2013) can also explain our observations of the MTZ anisotropy beneath the subduction zones.

4.3. The Effect of Anisotropy on MTZ Topography

We next explore how upper mantle and MTZ anisotropy affect the travel-times of SS precursors, an effect that has been neglected in previous MTZ topography studies. The MTZ topography can be biased by strong seismic anisotropy if the azimuthal distribution of SS bounce points is uniform in the region, a common scenario in many bins from our data set. Here, we apply an anisotropy correction based on surface wave anisotropy models to obtain a more precise MTZ topography model. First, we collect *Gc* and *Gs* values from the YB13SVani surface wave model (Yuan & Beghein, 2013) to compute velocity perturbations along each raypath using equations (1) and (2). Then, we use the same 1-D ray tracing technique as in section 2.3 to compute the travel-time residuals from PREM as a reference for the anisotropy corrections. After the anisotropy correction, we obtain a new MTZ topography model independent from upper mantle and MTZ anisotropy structures (Figure 12). The mean values of the 410, 660 depths and MTZ thickness remain almost the

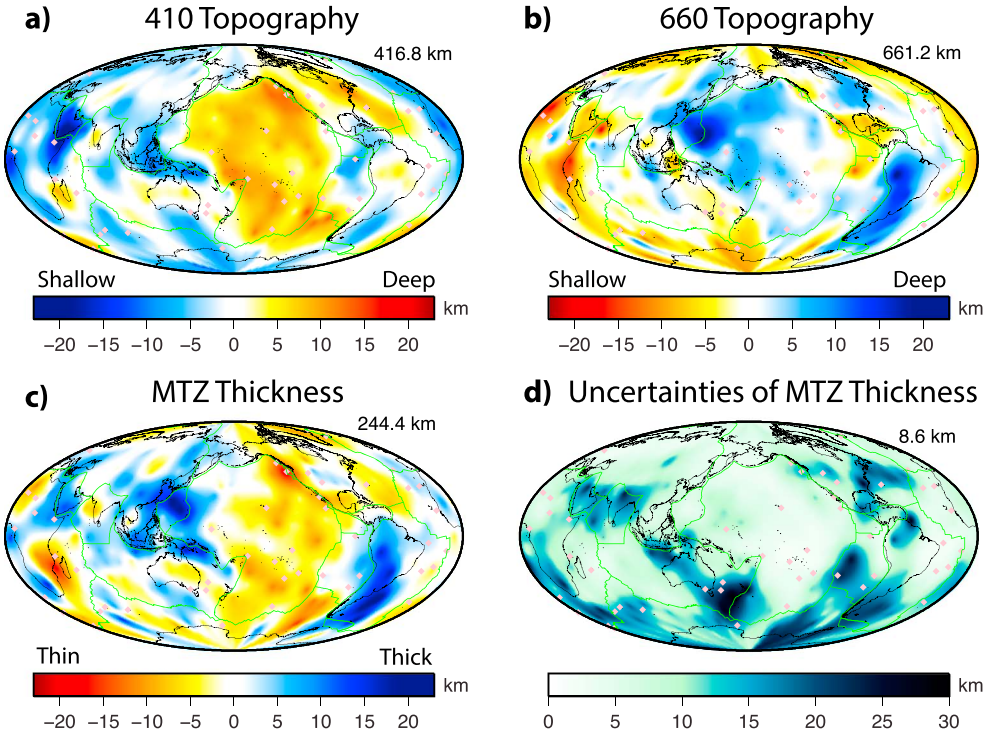

Figure 12. The MTZ topography model that is corrected for the upper mantle and MTZ anisotropy structures using YB13SVani model (Yuan & Beghein, 2013). The global map of (a) 410 topography, (b) 660 topography, (c) MTZ thickness, and (d) uncertainty of MTZ thickness. The legend is the same as Figure 4.

same after anisotropy correction (Figure 13). The mean values of the topography difference are all close to zero (Figures 13b, 13d, and 13f); the anisotropy correction results in only ±3 km topography difference, even smaller than the topography uncertainties.

The amplitude of 410 topography (Figure 13a) and MTZ thickness difference (Figure 13e) are smaller than that of 660 topography (Figure 13c), as S660S is affected by both the upper mantle and MTZ anisotropy structures. The Pacific and South America represent the areas with multiple MTZ topography studies. If we account for mantle anisotropy structures, the 410 and 660 depths would be ~2 km deeper in the western and southern Pacific, and ~4 km deeper in South America. The MTZ thickness would be thickened by ~3 km in southern East Pacific Rise and Izu-Bonin subduction zones and thickened by ~6 km in the Middle East. Regional studies of MTZ topography in the western and southern Pacific, and South America, should therefore incorporate an anisotropy correction to obtain a more precise topography model that is unbiased by anisotropy. Conversely, the difference in the central and northwestern Pacific is less than 1 km, which is negligible considering the uncertainties of topography.

We apply a spherical harmonic analysis to our MTZ topography model using a hierarchical Bayesian approach (Muir & Tkalčić, 2015). We find that the 410 topography has strong degree-1 power, while the 660 topography and MTZ thickness are both dominated by degree-2 power. This is consistent with previous global SS precursor studies (e.g., Gu et al., 2003; Houser et al., 2008). This also suggests that our MTZ topography model is characterized by long-wavelength structures such as the subduction zones in the western Pacific and South America and hot spots in the Pacific. These large-scale structures are in good agreement with previous global MTZ topography models, despite that different stacking and inversion techniques are applied (Deuss, 2009; Flanagan & Shearer, 1998; Gu et al., 2003; Houser et al., 2008; Lawrence & Shearer, 2006, 2008). Although long-wavelength structures agree, the small-scale structures have poor consistency among the models, especially in the Pacific. Some of these discrepancies have been noted before (e.g., Deuss, 2009; Lessing et al., 2015) as a result of using different bin sizes, filter selection and data regularization, and choice of tomography models for the corrections. Full 3-D waveform modeling (e.g., Chaljub & Tarantola, 1997; Bai et al., 2012; Koroni et al., 2017) coupled with large and carefully selected SS

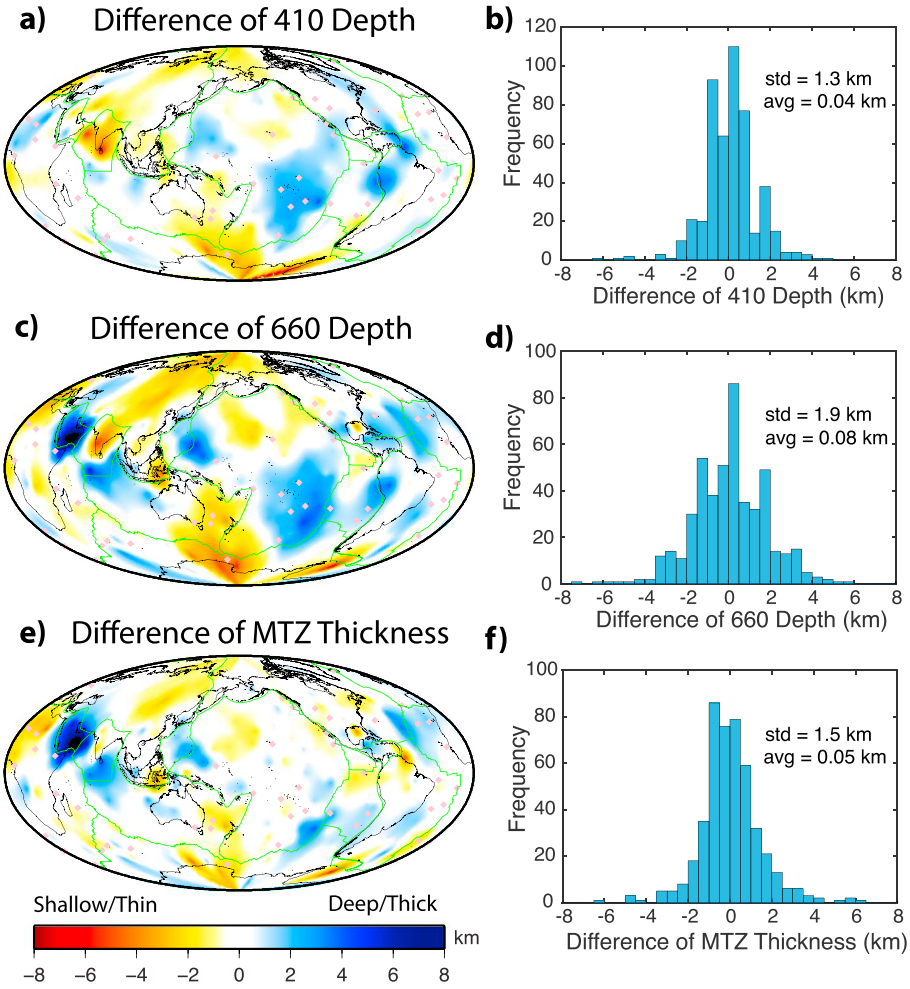

Figure 13. The difference of MTZ topography after the anisotropy correction. The map of the difference of (a) 410 topography, (c) 660 topography, and (e) MTZ thickness. The legend is the same as Figure 4. (b, d, and f) The histograms of the topography difference. The mean values (avg) and the standard deviations (std) are labeled in each panel.

waveform datasets will provide a way forward to both benchmark across methods and assist in interpreting smaller scale structures associated with mantle heterogeneities.

5. Conclusions

Using a large global data set of SS precursors, we have mapped the global MTZ structure for 410 and 660-km depths, MTZ thickness, and MTZ anisotropy. We find that the MTZ is thickened beneath subduction zones and thinned beneath hot spots; this is consistent with many previous studies and confirms that temperature plays a key role in the MTZ topography. We interrogate the azimuthal anisotropy in the upper mantle and transition zone at regional and global scales. In the central Pacific, we determine ~4% azimuthal anisotropy, with a SE fast direction in the upper mantle. We observe no significant azimuthal anisotropy within the MTZ beneath the central Pacific, consistent with a pattern of vertically dominated mantle flow in the MTZ. In the subduction zones, we detect ~4% anisotropy with a trench-parallel fast direction in the upper mantle. In the MTZ, we find ~3% anisotropy with a trench-perpendicular fast direction near slabs, which we attribute to the LPO of wadsleyite induced by the strong mantle flow near subduction zones. Globally, we observe ~1% azimuthal anisotropy in the upper mantle but no significant anisotropy in the MTZ. Thus, SS precursors suggest that the strength of azimuthal anisotropy in the MTZ is weaker than 1% at a global scale. We correct for upper mantle and MTZ anisotropy structures using surface wave anisotropy models, to obtain a more accurate MTZ topography model. The anisotropy correction corresponds to only ±3 km difference in the MTZ

topography, within the range of the uncertainties. However, the regional studies of MTZ topography in the western Pacific, southern Pacific, and South America require corrections for the upper mantle and MTZ anisotropy structures.

Acknowledgments
The SS data set was downloaded from Incorporated Research Institutions for Seismology, Data Management Center (IRIS DMC). The SS data set and MTZ topography model are available at http://hdl.handle.net/1903/21819 (DOI: https://doi.org/10.13016/3ecr-1hsu). We thank the Editors and two anonymous reviewers for constructive comments and suggestions. We also thank Vedran Lekić for helpful discussions about spherical harmonic analysis and anisotropy inversions. Q. H., L. W., and N. S. were supported by National Science Foundation (NSF) Grant EAR-1447041. L. W. is the recipient of a Discovery Early Career Research Award (DE170100329) funded by the Australian Government. C. B. was supported by NSF Grant EAR-1446978.

References

Bai, L., Zhang, Y., & Ritsema, J. (2012). An analysis of SS precursors using spectral-element method seismograms. *Geophysical Journal International*, *188*(1), 293–300. http://doi.org/10.1111/j.1365-246X.2011.05256.x

Bass, J. D., & Kanzaki, M. (1990). Elasticity of a majorite-pyrope solid solution. *Geophysical Research Letters*, *17*(11), 1989–1992. http://doi.org/10.1029/GL017i011p01989

Bassin, C., Laske, G., & Masters, G. (2000). The current limits of resolution for surface wave tomography in North America. EOS Trans. AGU. 81: Fall Meet. Suppl., Abstract.

Becker, T. W., Lebedev, S., & Long, M. D. (2012). On the relationship between azimuthal anisotropy from shear wave splitting and surface wave tomography. *Journal of Geophysical Research*, *117*, B01306. http://doi.org/10.1029/2011JB008705

Becker, T. W., Schaeffer, A. J., Lebedev, S., & Conrad, C. P. (2015). Toward a generalized plate motion reference frame. *Geophysical Research Letters*, *42*, 3188–3196. http://doi.org/10.1002/2015GL063695

Beghein, C., Resovsky, J., & van der Hilst, R. D. (2008). The signal of mantle anisotropy in the coupling of normal modes. *Geophysical Journal International*, *175*(3), 1209–1234. http://doi.org/10.1111/j.1365-246X.2008.03970.x

Beghein, C., & Trampert, J. (2004). Probability density functions for radial anisotropy: Implications for the upper 1200 km of the mantle. *Earth and Planetary Science Letters*, *217*(1-2), 151–162. http://doi.org/10.1016/S0012-821X(03)00575-2

Bercovici, D., & Karato, S.-I. (2003). Whole-mantle convection and the transition-zone water filter. *Nature*, *425*(6953), 39–44. http://doi.org/10.1038/nature01918

Billen, M. I. (2008). Modeling the dynamics of subducting slabs. *Annual Review of Earth and Planetary Sciences*, *36*(1), 325–356. http://doi.org/10.1146/annurev.earth.36.031207.124129

Billen, M. I. (2010). Slab dynamics in the transition zone. *Physics of the Earth and Planetary Interiors*, *183*(1-2), 296–308. http://doi.org/10.1016/j.pepi.2010.05.005

Bina, C. R., & Helffrich, G. (1994). Phase transition Clapeyron slopes and transition zone seismic discontinuity topography. *Journal of Geophysical Research*, *99*(B8), 15,853–15,860. http://doi.org/10.1029/94JB00462

Cao, Q., Van der Hilst, R. D., De Hoop, M. V., & Shim, S. H. (2011). Seismic imaging of transition zone discontinuities suggests hot mantle west of Hawaii. *Science*, *332*(6033), 1068–1071. http://doi.org/10.1126/science.1202731

Chaljub, E., & Tarantola, A. (1997). Sensitivity of SS precursors to topography on the upper-mantle 660-km discontinuity. *Geophysical Research Letters*, *24*(21), 2613–2616. http://doi.org/10.1029/97GL52693

Chambers, K., Woodhouse, J. H., & Deuss, A. (2005). Topography of the 410-km discontinuity from PP and SS precursors. *Earth and Planetary Science Letters*, *235*(3-4), 610–622. http://doi.org/10.1016/j.epsl.2005.05.014

Chang, S.-J., Ferreira, A. M. G., Ritsema, J., van Heijst, H. J., & Woodhouse, J. H. (2015). Joint inversion for global isotropic and radially anisotropic mantle structure including crustal thickness perturbations. *Journal of Geophysical Research: Solid Earth*, *120*, 4278–4300. http://doi.org/10.1002/2014JB011824

Chen, W. P., & Brudzinski, M. R. (2003). Seismic anisotropy in the mantle transition zone beneath Fiji-Tonga. *Geophysical Research Letters*, *30*(13), 1682. http://doi.org/10.1029/2002GL016330

Courtier, A. M., Jackson, M. G., Lawrence, J. F., Wang, Z., Lee, C.-T. A., Halama, R., et al. (2007). Correlation of seismic and petrologic thermometers suggests deep thermal anomalies beneath hotspots. *Earth and Planetary Science Letters*, *264*(1-2), 308–316. http://doi.org/10.1016/j.epsl.2007.10.003

Courtillot, V., Davaille, A., Besse, J., & Stock, J. (2003). Three distinct types of hotspots in the Earth's mantle. *Earth and Planetary Science Letters*, *205*(3-4), 295–308. http://doi.org/10.1016/S0012-821X(02)01048-8

Crampin, S. (1984). An introduction to wave propagation in anisotropic media. *Geophysical Journal International*, *76*(1), 17–28. http://doi.org/10.1111/j.1365-246X.1984.tb05018.x

Debayle, E., Dubuffet, F., & Durand, S. (2016). An automatically updated S-wave model of the upper mantle and the depth extent of azimuthal anisotropy. *Geophysical Research Letters*, *43*, 674–682. http://doi.org/10.1002/2015GL067329

DeMets, C., Gordon, R. G., Argus, D. F., & Stein, S. (1990). Current plate motions. *Geophysical Journal International*, *101*(2), 425–478. http://doi.org/10.1111/j.1365-246X.1990.tb06579.x

Deuss, A. (2009). Global observations of mantle discontinuities using SS and PP precursors. *Surveys in Geophysics*, *30*(4-5), 301–326. http://doi.org/10.1007/s10712-009-9078-y

Deuss, A., & Woodhouse, J. H. (2002). A systematic search for mantle discontinuities using SS-precursors. *Geophysical Research Letters*, *29*(8), 1249. http://doi.org/10.1029/2002GL014768

Dziewonski, A. M., & Anderson, D. L. (1981). Preliminary reference Earth model. *Physics of the Earth and Planetary Interiors*, *25*(4), 297–356. http://doi.org/10.1016/0031-9201(81)90046-7

Efron, B., & Tibshirani, R. (1986). Bootstrap methods for standard errors, confidence intervals, and other measures of statistical accuracy. *Statistical Science*. http://doi.org/10.2307/2245500

Ekström, G., & Dziewonski, A. M. (1998). The unique anisotropy of the Pacific upper mantle. *Nature*, *394*(6689), 168–172. http://doi.org/10.1038/28148

Flanagan, M. P., & Shearer, P. M. (1998). Global mapping of topography on transition zone velocity discontinuities by stacking SS precursors. *Journal of Geophysical Research*, *103*(B2), 2673–2692. http://doi.org/10.1029/97JB03212

Flanagan, M. P., & Shearer, P. M. (1999). A map of topography on the 410-km discontinuity from PP precursors. *Geophysical Research Letters*, *26*(5), 549–552. http://doi.org/10.1029/1999GL900036

Foley, B. J., & Long, M. D. (2011). Upper and mid-mantle anisotropy beneath the Tonga slab. *Geophysical Research Letters*, *38*, L02303. http://doi.org/10.1029/2010GL046021

Fouch, M. J., & Fischer, K. M. (1996). Mantle anisotropy beneath northwest Pacific subduction zones. *Journal of Geophysical Research*, *101*(B7), 15,987–16,002. http://doi.org/10.1029/96JB00881

French, S. W., & Romanowicz, B. A. (2014). Whole-mantle radially anisotropic shear velocity structure from spectral-element waveform tomography. *Geophysical Journal International*, *199*(3), 1303–1327. http://doi.org/10.1093/gji/ggu334

Friederich, W., & Dalkolmo, J. (1995). Complete synthetic seismograms for a spherically symmetric Earth by a numerical computation of the Green's function in the frequency domain. *Geophysical Journal International*, *122*(2), 537–550. http://doi.org/10.1111/j.1365-246X.1995.tb07012.x

Fukao, Y., Widiyantoro, S., & Obayashi, M. (2001). Stagnant slabs in the upper and lower mantle transition region. *Reviews of Geophysics*, *39*(3), 291–323. http://doi.org/10.1029/1999RG000068

Gu, Y., Dziewonski, A. M., & Agee, C. B. (1998). Global de-correlation of the topography of transition zone discontinuities. *Earth and Planetary Science Letters*, *157*(1-2), 57–67. http://doi.org/10.1016/S0012-821X(98)00027-2

Gu, Y. J., & Dziewonski, A. M. (2002). Global variability of transition zone thickness. *Journal of Geophysical Research*, *107*(B7), 2135. http://doi.org/10.1029/2001JB000489

Gu, Y. J., Dziewonski, A. M., & Ekström, G. (2003). Simultaneous inversion for mantle shear velocity and topography of transition zone discontinuities. *Geophysical Journal International*, *154*(2), 559–583. http://doi.org/10.1046/j.1365-246X.2003.01967.x

Hayes, G. P., Wald, D. J., & Johnson, R. L. (2012). Slab1.0: A three-dimensional model of global subduction zone geometries. *Journal of Geophysical Research*, *117*, B01302. http://doi.org/10.1029/2011JB008524

Heit, B., Yuan, X., Bianchi, M., Kind, R., & Gossler, J. (2010). Study of the lithospheric and upper-mantle discontinuities beneath eastern Asia by SS precursors. *Geophysical Journal International*, *183*(1), 252–266. http://doi.org/10.1111/j.1365-246X.2010.04714.x

Helffrich, G. (2000). Topography of the transition zone seismic discontinuities. *Reviews of Geophysics*, *38*(1), 141–158. http://doi.org/10.1029/1999RG000060

Houser, C., Masters, G., Flanagan, M., & Shearer, P. (2008). Determination and analysis of long-wavelength transition zone structure using SS precursors. *Geophysical Journal International*, *174*(1), 178–194. http://doi.org/10.1111/j.1365-246X.2008.03719.x

Ita, J., & Stixrude, L. (1992). Petrology, elasticity, and composition of the mantle transition zone. *Journal of Geophysical Research*, *97*(B5), 6849–6866. http://doi.org/10.1029/92JB00068

Ito, E., & Takahashi, E. (1989). Postspinel transformations in the system Mg_2SiO_4-Fe_2SiO_4 and some geophysical implications. *Journal of Geophysical Research*, *94*(B8), 10,637–10,646. http://doi.org/10.1029/JB094iB08p10637

Karato, S. (1988). The role of recrystallization in the preferred orientation of olivine. *Physics of the Earth and Planetary Interiors*, *51*(1-3), 107–122. http://doi.org/10.1016/0031-9201(88)90029-5

Karato, S.-I., Jung, H., Katayama, I., & Skemer, P. (2008). Geodynamic significance of seismic anisotropy of the upper mantle: New insights from laboratory studies. *Annual Review of Earth and Planetary Sciences*, *36*(1), 59–95. http://doi.org/10.1146/annurev.earth.36.031207.124120

Katsura, T., & Ito, E. (1989). The system Mg_2SiO_4-Fe_2SiO_4 at high pressures and temperatures: Precise determination of stabilities of olivine, modified spinel, and spinel. *Journal of Geophysical Research*, *94*(B11), 15,663–15,670. http://doi.org/10.1029/JB094iB11p15663

Kawazoe, T., Ohuchi, T., Nishihara, Y., Nishiyama, N., Fujino, K., & Irifune, T. (2013). Seismic anisotropy in the mantle transition zone induced by shear deformation of wadsleyite. *Physics of the Earth and Planetary Interiors*, *216*, 91–98. http://doi.org/10.1016/j.pepi.2012.12.005

Kennett, B. L. N., Engdahl, E. R., & Buland, R. (1995). Constraints on seismic velocities in the Earth from traveltimes. *Geophysical Journal International*, *122*(1), 108–124. http://doi.org/10.1111/j.1365-246X.1995.tb03540.x

Kiefer, B., Stixrude, L., & Wentzcovitch, R. M. (1997). Calculated elastic constants and anisotropy of Mg_2SiO_4 spinel at high pressure. *Geophysical Research Letters*, *24*(22), 2841–2844. http://doi.org/10.1029/97GL02975

Koroni, M., Bozdag, E., Paulssen, H., & Trampert, J. (2017). Sensitivity analysis of seismic waveforms to upper-mantle discontinuities using the adjoint method. *Geophysical Journal International*, *210*(3), 1965–1980. http://doi.org/10.1093/gji/ggx286

Koroni, M., & Trampert, J. (2016). The effect of topography of upper-mantle discontinuities on SS precursors. *Geophysical Journal International*, *204*(1), 667–681. http://doi.org/10.1093/gji/ggv471

Lawrence, J. F., & Shearer, P. M. (2006). Constraining seismic velocity and density for the mantle transition zone with reflected and transmitted waveforms. *Geochemistry, Geophysics, Geosystems*, *7*, Q10012. http://doi.org/10.1029/2006GC001339

Lawrence, J. F., & Shearer, P. M. (2008). Imaging mantle transition zone thickness with SdS-SS finite-frequency sensitivity kernels. *Geophysical Journal International*, *174*(1), 143–158. http://doi.org/10.1111/j.1365-246X.2007.03673.x

Lekić, V., & Romanowicz, B. (2011). Inferring upper-mantle structure by full waveform tomography with the spectral element method. *Geophysical Journal International*, *185*(2), 799–831. http://doi.org/10.1111/j.1365-246X.2011.04969.x

Lessing, S., Thomas, C., Rost, S., Cobden, L., & Dobson, D. P. (2014). Mantle transition zone structure beneath India and Western China from migration of PP and SS precursors. *Geophysical Journal International*, *197*(1), 396–413. http://doi.org/10.1093/gji/ggt511

Lessing, S., Thomas, C., Saki, M., Schmerr, N., & Vanacore, E. (2015). On the difficulties of detecting PP precursors. *Geophysical Journal International*, *201*(3), 1666–1681. http://doi.org/10.1093/gji/ggv105

Li, J., Zheng, Y., Thomsen, L., Lapen, T. J., & Fang, X. (2018). Deep earthquakes in subducting slabs hosted in highly anisotropic rock fabric. *Nature Geoscience*, *11*(9), 696–700. http://doi.org/10.1038/s41561-018-0188-3

Li, L., Weidner, D. J., Brodholt, J., Alfè, D., & Price, G. D. (2006). Elasticity of Mg_2SiO_4 ringwoodite at mantle conditions. *Physics of the Earth and Planetary Interiors*, *157*(3-4), 181–187. http://doi.org/10.1016/j.pepi.2006.04.002

Long, M. D., & Silver, P. G. (2008). The subduction zone flow field from seismic anisotropy: A global view. *Science*, *319*(5861), 315–318. http://doi.org/10.1126/science.1150809

Long, M. D., & Silver, P. G. (2009). Mantle flow in subduction systems: The subslab flow field and implications for mantle dynamics. *Journal of Geophysical Research*, *114*, Q05S15. http://doi.org/10.1029/2008JB006200

Long, M. D., & Wirth, E. A. (2013). Mantle flow in subduction systems: The mantle wedge flow field and implications for wedge processes. *Journal of Geophysical Research: Solid Earth*, *118*, 583–606. http://doi.org/10.1002/jgrb.50063

Mainprice, D. (2007). Seismic anisotropy of the deep Earth from a mineral and rock physics perspective. *Treatise in Geophysics Volume*, *2*, 437–492.

Mainprice, D., Tommasi, A., Couvy, H., Cordier, P., & Frost, D. J. (2005). Pressure sensitivity of olivine slip systems and seismic anisotropy of Earth's upper mantle. *Nature*, *433*(7027), 731–733. http://doi.org/10.1038/nature03266

Montagner, J. P. (2002). Upper mantle low anisotropy channels below the Pacific Plate. *Earth and Planetary Science Letters*, *202*(2), 263–274. http://doi.org/10.1016/S0012-821X(02)00791-4

Montagner, J.-P., Griot Pommera, D. A., & Lavé, J. (2000). How to relate body wave and surface wave anisotropy? *Journal of Geophysical Research*, *105*(B8), 19,015–19,027. http://doi.org/10.1029/2000JB900015

Montagner, J.-P., & Nataf, H. C. (1986). A simple method for inverting the azimuthal anisotropy of surface waves. *Journal of Geophysical Research*, *91*(B1), 511–520. http://doi.org/10.1029/JB091iB01p00511

Moulik, P., & Ekström, G. (2014). An anisotropic shear velocity model of the Earth's mantle using normal modes, body waves, surface waves and long-period waveforms. *Geophysical Journal International*, *199*(3), 1713–1738. http://doi.org/10.1093/gji/ggu356

Muir, J. B., & Tkalčić, H. (2015). A method of spherical harmonic analysis in the geosciences via hierarchical Bayesian inference. *Geophysical Journal International*, *203*(2), 1164–1171. http://doi.org/https://doi.org/10.1093/gji/ggv361

Nishimura, C. E., & Forsyth, D. W. (1989). The anisotropic structure of the upper mantle in the Pacific. *Geophysical Journal International*, *96*(2), 203–229. http://doi.org/10.1111/j.1365-246X.1989.tb04446.x

Pamato, M. G., Kurnosov, A., Boffa Ballaran, T., Frost, D. J., Ziberna, L., Giannini, M., et al. (2016). Single crystal elasticity of majoritic garnets: Stagnant slabs and thermal anomalies at the base of the transition zone. *Earth and Planetary Science Letters*, *451*, 114–124. http://doi.org/10.1016/j.epsl.2016.07.019

Revenaugh, J. S., & Jordan, T. H. (1991). Mantle layering from ScS reverberation: 2. The transition zone. *Journal of Geophysical Research*, *96*(B12), 19,763–19,780. http://doi.org/https://doi.org/10.1029/91JB01486

Ringwood, A. E. (1975). *Composition and petrology of the Earth's mantle*, (p. 618). New York: McGraw-Hill.

Ritsema, J., Deuss, A., van Heijst, H. J., & Woodhouse, J. H. (2011). S40RTS: A degree-40 shear-velocity model for the mantle from new Rayleigh wave dispersion, teleseismic traveltime and normal-mode splitting function measurements. *Geophysical Journal International*, *184*(3), 1223–1236. http://doi.org/10.1111/j.1365-246X.2010.04884.x

Rychert, C. A., Harmon, N., & Schmerr, N. (2014). Synthetic waveform modelling of SS precursors from anisotropic upper-mantle discontinuities. *Geophysical Journal International*, *196*(3), 1694–1705. http://doi.org/10.1093/gji/ggt474

Rychert, C. A., Schmerr, N., & Harmon, N. (2012). The Pacific lithosphere-asthenosphere boundary: Seismic imaging and anisotropic constraints from SS waveforms. *Geochemistry, Geophysics, Geosystems*, *13*, Q0AK10. http://doi.org/10.1029/2012GC004194

Saki, M., Thomas, C., Merkel, S., & Wookey, J. (2018). Detecting seismic anisotropy above the 410 km discontinuity using reflection coefficients of underside reflections. *Physics of the Earth and Planetary Interiors*, *274*, 170–183. http://doi.org/10.1016/j.pepi.2017.12.001

Sang, L., & Bass, J. D. (2014). Single-crystal elasticity of diopside to 14 GPa by Brillouin scattering. *Physics of the Earth and Planetary Interiors*, *228*, 75–79. http://doi.org/10.1016/j.pepi.2013.12.011

Sawamoto, H., Weidner, D. J., Sasaki, S., & Kumazawa, M. (1984). Single-crystal elastic properties of the modified spinal (beta) phase of magnesium orthosilicate. *Science*, *224*(4650), 749–751. http://doi.org/10.1126/science.224.4650.749

Schaeffer, A. J., Lebedev, S., & Becker, T. W. (2016). Azimuthal seismic anisotropy in the Earth's upper mantle and the thickness of tectonic plates. *Geophysical Journal International*, *207*(2), 901–933. http://doi.org/10.1093/gji/ggw309

Schmerr, N., & Garnero, E. (2006). Investigation of upper mantle discontinuity structure beneath the central Pacific using SS precursors. *Journal of Geophysical Research*, *111*, B08305. http://doi.org/10.1029/2005JB004197

Schmerr, N., Garnero, E., & McNamara, A. (2010). Deep mantle plumes and convective upwelling beneath the Pacific Ocean. *Earth and Planetary Science Letters*, *294*(1-2), 143–151. http://doi.org/10.1016/j.epsl.2010.03.014

Schmerr, N., & Garnero, E. J. (2007). Upper mantle discontinuity topography from thermal and chemical heterogeneity. *Science*, *318*(5850), 623–626. http://doi.org/10.1126/science.1145962

Shearer, P. M. (1991). Constraints on upper mantle discontinuities from observations of long-period reflected and converted phases. *Journal of Geophysical Research*, *96*(B11), 18,147–18,182. http://doi.org/10.1029/91JB01592

Shearer, P. M. (1993). Global mapping of upper mantle reflectors from long-period SS precursors. *Geophysical Journal International*, *115*(3), 878–904. http://doi.org/10.1111/j.1365-246X.1993.tb01499.x

Sinogeikin, S. V., Bass, J. D., & Katsura, T. (2003). Single-crystal elasticity of ringwoodite to high pressures and high temperatures: Implications for 520 km seismic discontinuity. *Physics of the Earth and Planetary Interiors*, *136*(1-2), 41–66. http://doi.org/10.1016/S0031-9201(03)00022-0

Sinogeikin, S. V., Katsura, T., & Bass, J. D. (1998). Sound velocities and elastic properties of Fe-bearing wadsleyite and ringwoodite. *Journal of Geophysical Research*, *103*(B9), 20,819–20,825. http://doi.org/10.1029/98JB01819

Stixrude, L. (1997). Structure and sharpness of phase transitions and mantle discontinuities. *Journal of Geophysical Research*, *102*(B7), 14,835–14,852. http://doi.org/10.1029/97JB00550

Thomas, C., & Billen, M. I. (2009). Mantle transition zone structure along a profile in the SW Pacific: Thermal and compositional variations. *Geophysical Journal International*, *176*(1), 113–125. http://doi.org/10.1111/j.1365-246X.2008.03934.x

Tommasi, A., Mainprice, D., Cordier, P., Thoraval, C., & Couvy, H. (2004). Strain-induced seismic anisotropy of wadsleyite polycrystals and flow patterns in the mantle transition zone. *Journal of Geophysical Research*, *109*, B12405. http://doi.org/10.1029/2004JB003158

Tong, C., Gudmundsson, O., & Kennett, B. L. N. (1994). Shear wave splitting in refracted waves returned from the upper mantle transition zone beneath northern Australia. *Journal of Geophysical Research*, *99*(B8), 15,783–15,797. http://doi.org/10.1029/94JB00460

Trampert, J., & van Heijst, H. J. (2002). Global azimuthal anisotropy in the transition zone. *Science*, *296*(5571), 1297–1299. http://doi.org/10.1126/science.1070264

Waszek, L., Schmerr, N. C., & Ballmer, M. D. (2018). Global observations of reflectors in the mid-mantle with implications for mantle structure and dynamics. *Nature Communications*, *9*(1), 385. http://doi.org/10.1038/s41467-017-02709-4

Webb, S. L. (1989). The elasticity of the upper mantle orthosilicates olivine and garnet to 3 GPa. *Physics and Chemistry of Minerals*, *16*(7), 684–692. http://doi.org/10.1007/BF00223318

Weidner, D. J., Sawamoto, H., Sasaki, S., & Kumazawa, M. (1984). Single-crystal elastic properties of the spinel phase of Mg_2SiO_4. *Journal of Geophysical Research*, *89*(B9), 7852–7860. http://doi.org/10.1029/JB089iB09p07852

Wookey, J., Kendall, J. M., & Barruol, G. (2002). Mid-mantle deformation inferred from seismic anisotropy. *Nature*, *415*(6873), 777–780. http://doi.org/10.1038/415777a

Yang, J., Mao, Z., Lin, J.-F., & Prakapenka, V. B. (2014). Single-crystal elasticity of the deep-mantle magnesite at high pressure and temperature. *Earth and Planetary Science Letters*, *392*, 292–299. http://doi.org/10.1016/j.epsl.2014.01.027

Yu, C., Day, E. A., de Hoop, M. V., Campillo, M., & van der Hilst, R. D. (2017). Mapping mantle transition zone discontinuities beneath the central Pacific with array processing of SS precursors. *Journal of Geophysical Research: Solid Earth*, *122*, 10,364–10,378. http://doi.org/10.1002/2017JB014327

Yuan, K., & Beghein, C. (2013). Seismic anisotropy changes across upper mantle phase transitions. *Earth and Planetary Science Letters*, *374*, 132–144. http://doi.org/10.1016/j.epsl.2013.05.031

Yuan, K., & Beghein, C. (2014). Three-dimensional variations in Love and Rayleigh wave azimuthal anisotropy for the upper 800 km of the mantle. *Journal of Geophysical Research: Solid Earth*, *119*, 3232–3255. http://doi.org/10.1002/2013JB010853

Yuan, K., & Beghein, C. (2018). A Bayesian method to quantify azimuthal anisotropy model uncertainties: Application to global azimuthal anisotropy in the upper mantle and transition zone. *Geophysical Journal International*, *213*(1), 603–622. http://doi.org/10.1093/gji/ggy004

Zha, C. S., Duffy, T. S., Mao, H. K., Downs, R. T., Hemley, R. J., & Weidner, D. J. (1997). Single-crystal elasticity of β-Mg_2SiO_4 to the pressure of the 410 km seismic discontinuity in the Earth's mantle. *Earth and Planetary Science Letters*, *147*(1-4), E9–E15. http://doi.org/10.1016/S0012-821X(97)00010-1

Zhang, J. S., Bass, J. D., & Schmandt, B. (2018). The elastic anisotropy change near the 410-km discontinuity: Predictions from single-crystal elasticity measurements of olivine and wadsleyite. *Journal of Geophysical Research: Solid Earth*, *123*, 2674–2684. http://doi.org/10.1002/2017JB015339

Zhao, L., & Chevrot, S. (2003). SS-wave sensitivity to upper mantle structure: Implications for the mapping of transition zone discontinuity topographies. *Geophysical Research Letters*, *30*(11), 1590. http://doi.org/10.1029/2003GL017223